PHYSICAL REVIEW D **82,** 075010 (2010)

Proposals for bottom quark/squark renormalization in the complex MSSM

S. Heinemeyer,[1,*] H. Rzehak,[2,†] and C. Schappacher[2,‡]
[1]*Instituto de Física de Cantabria (CSIC-UC), Santander, Spain*
[2]*Institut für Theoretische Physik, Karlsruhe Institute of Technology, D–76128 Karlsruhe, Germany*
(Received 14 July 2010; published 14 October 2010)

We present a consistent renormalization of the top- and bottom-quark/squark sector of the minimal supersymmetric standard model with complex parameters. Various renormalization schemes are defined, analyzed analytically, and tested numerically in the decays $\tilde{t}_2 \to \tilde{b}_i H^+/W^+$ $(i = 1, 2)$. No scheme is found that produces numerically acceptable results over all the parameter space, where problems occur in most cases already for real parameters. Two schemes are identified that show the most robust behavior. A numerical analysis of the four partial stop decay widths is performed in our "preferred" scheme, "m_b, A_b $\overline{\text{DR}}$." The full one-loop corrections to the corresponding partial decay widths are evaluated, including hard QED and QCD radiation. We find mostly modest corrections at the one-loop level.

DOI: 10.1103/PhysRevD.82.075010 PACS numbers: 14.80.Ly, 11.10.Gh, 11.30.Pb

I. INTRODUCTION

One of the main tasks of the LHC is to search for supersymmetry (SUSY) [1]. The minimal supersymmetric standard model (MSSM) predicts two scalar partners for all standard model (SM) fermions as well as fermionic partners to all SM bosons. Of particular interest are the scalar partners of the heavy SM quarks, the scalar top quarks, $\tilde{t}_i$ $(i = 1, 2)$ and scalar bottom quarks $\tilde{b}_j$ $(j = 1, 2)$ due to their large Yukawa couplings. A scalar top quark $\tilde{t}_i$ has many possible decay modes, depending on the mass patterns of the SUSY particles. Among those decay modes are the decays to a scalar bottom quark, $\tilde{b}_j$, and a charged Higgs boson, H^+, or W boson, W^+,

$$\tilde{t}_i \to \tilde{b}_j H^+ \qquad (i, j = 1, 2), \tag{1}$$

$$\tilde{t}_i \to \tilde{b}_j W^+ \qquad (i, j = 1, 2). \tag{2}$$

If these channels are kinematically allowed they can even be dominant if (most of) the other decay modes are kinematically forbidden. Consequently, these processes can constitute a large part of the total stop decay width, and, in case of decays to a Higgs boson, they can serve as a source of charged Higgs bosons in cascade decays at the LHC.

For a precise prediction of the partial decay widths corresponding to Eq. (1) and (2), at least the one-loop level contributions have to be taken into account. This in turn requires a renormalization of the relevant sectors, especially a simultaneous renormalization of the top- and bottom-quark/squark sector. Because of the $SU(2)_L$ invariance of the left-handed scalar top and bottom quarks, these two sectors cannot be treated independently. Within the framework of the MSSM with complex parameters (cMSSM) we analyze various bottom-quark/squark sector renormalization schemes, while we apply a commonly used on-shell (OS) renormalization scheme for the top-quark/squark sector throughout all the investigations. Special attention is paid to "perturbativity," i.e. the loop corrections should not be enhanced by large counterterm contributions resulting from an inappropriate renormalization scheme. This turns out to be a constraint that is very difficult to fulfill over the whole cMSSM parameter range, where it is especially difficult to achieve this simultaneously for small and large values of $\tan\beta$.

Higher-order corrections to scalar fermion decays have been evaluated in various analysis over the last decade. The simultaneous renormalization of the top- and the bottom-quark/squark sector was taken into account only in a relatively small subset. In Refs. [2,3] stop and sbottom decays, including the ones to charged Higgs and SM gauge bosons, have been evaluated at $\mathcal{O}(\alpha_s)$ within the MSSM with real parameters (rMSSM). The numerical investigation was restricted to relatively low $\tan\beta$ values. These calculations are implemented in the program SDECAY [4]. A similar analysis in Ref. [5] included electroweak one-loop corrections, where again only relatively low $\tan\beta$ values were considered. The decays of Higgs bosons to scalar fermions, including the charged Higgs decays, at the full one-loop level within the rMSSM was presented in Refs. [6,7], indicating very large one-loop corrections for large $\tan\beta$. An effective Lagrangian approach in the rMSSM for these types of decays was given in Ref. [8], with a numerical analysis for $\tan\beta = 5$.

The renormalization of the top- and bottom-quark/squark sector has been analyzed also in the context of other calculations in the past. A comparison of different renormalization schemes within the rMSSM was performed in Refs. [9,10], focusing on large $\tan\beta$. One of the renormalization schemes considered therein had

*Sven.Heinemeyer@cern.ch
†hr@particle.uni-karlsruhe.de
‡cs@particle.uni-karlsruhe.de

been used before within the calculation of the two-loop bottom-quark/squark contributions to the neutral Higgs boson masses [11] which are important for large $\tan\beta$ values. Within the cMSSM a renormalization was presented in Ref. [12], however without an analysis of its practicability. In Refs. [9,13] the top- and bottom-quark/squark sector was renormalized within the cMSSM, but only the QCD part needed for the presented calculation was considered. Thus, no complete top- and bottom-quark/squark sector renormalization has been performed within the cMSSM. Recently a renormalization of nearly all sectors of the rMSSM appeared [14]. In this analysis, however, the main focus has been on gauge parameter independence.

Complex phases, as assumed here in the cMSSM, can be relevant for collider observables and possibly extracted from experimental data. Scalar top-quark branching ratios at a linear collider are discussed in Ref. [15]. Concerning LHC measurements, triple products involving the decay of scalar top or bottom quarks are analyzed in Refs. [16–20]. Finally, rate asymmetries are examined in Ref. [21]. Depending on assumptions about the LHC performance it might be possible to extract information on the phases of M_1, A_t, and A_b at the LHC.

In this paper we analyze the renormalization of the full top- and bottom-quark/squark sector in the cMSSM. We show analytically (and numerically) why certain renormalization schemes fail for specific parts of the parameter space. Finally, we explore the one-loop effects for the decays (1) and (2) for important parts of the cMSSM parameter space in the favored renormalization scheme. We present numerical results showing the size of the one-loop corrections, especially including small and large $\tan\beta$. The evaluation of the partial decay widths of the scalar top quarks are being implemented into the Fortran code FEYNHIGGS [22–25]. A numerical analysis of *all* scalar top-quark decay modes, involving a renormalization of *all* relevant sectors will be presented elsewhere [26].

II. THE GENERIC STRUCTURE OF THE QUARK/SQUARK SECTOR

The decay channels (1) and (2) are calculated at the full one-loop level (including hard QED and QCD radiation). This requires the renormalization of several sectors of the cMSSM as discussed below. The sectors not discussed in detail are renormalized as follows:

(i) The gauge and Higgs sector renormalization has been performed following Ref. [25]. The gauge boson masses, M_W and M_Z, as well as the mass of the charged Higgs boson, $M_H^\pm$, has been defined on shell while the sine squared of the weak mixing angle, $s_{\rm w}^2$, is defined via the gauge boson masses, $s_{\rm w}^2 = 1 - M_W^2/M_Z^2$. The Z factors for the W boson field are also determined within an on-shell scheme while the Z factors of the charged Higgs boson field are given by a linear combination of the $\overline{\rm DR}$ Z factors of the Higgs doublets (see Ref. [25]). An additional finite Z factor is introduced to fulfill on-shell conditions for the external charged $H^\pm$ field. $\tan\beta$ is defined as $\overline{\rm DR}$ parameter.

(ii) The Higgs mixing parameter μ has been renormalized via an OS procedure for the neutralino and chargino sector [12,27].

(iii) For the renormalization of the electromagnetic charge we require that the renormalized $ee\gamma$ vertex in the Thomson limit is not changed by higher-order corrections with respect to the corresponding tree-level vertex [28].

A detailed description of our renormalization of all sectors will be given in Ref. [26].

In the following we focus on the top- and bottom-quark/squark sector. The bilinear part of the Lagrangian with top- and bottom-squark fields, $\tilde{t}$ and $\tilde{b}$,

$$\mathcal{L}_{\tilde{t}/\tilde{b}\,\rm mass} = -\left(\tilde{t}_L^\dagger, \tilde{t}_R^\dagger\right)\mathbf{M}_{\tilde{t}}\begin{pmatrix}\tilde{t}_L\\ \tilde{t}_R\end{pmatrix} - \left(\tilde{b}_L^\dagger, \tilde{b}_R^\dagger\right)\mathbf{M}_{\tilde{b}}\begin{pmatrix}\tilde{b}_L\\ \tilde{b}_R\end{pmatrix}, \quad (3)$$

contains the stop and sbottom mass matrices $\mathbf{M}_{\tilde{t}}$ and $\mathbf{M}_{\tilde{b}}$, given by

$$\mathbf{M}_{\tilde{q}} = \begin{pmatrix} M_{\tilde{Q}_L}^2 + m_q^2 + M_Z^2 c_{2\beta}(T_q^3 - Q_q s_{\rm w}^2) & m_q X_q^* \\ m_q X_q & M_{\tilde{q}_R}^2 + m_q^2 + M_Z^2 c_{2\beta} Q_q s_{\rm w}^2 \end{pmatrix}, \quad (4)$$

with

$$X_q = A_q - \mu^* \kappa, \quad \kappa = \{\cot\beta, \tan\beta\} \ \text{for}\ q = \{t, b\}. \quad (5)$$

$M_{\tilde{Q}_L}^2$ and $M_{\tilde{q}_R}^2$ are the soft SUSY-breaking mass parameters. m_q is the mass of the corresponding quark. Q_q and T_q^3 denote the charge and the isospin of q, and A_q is the trilinear soft SUSY-breaking parameter. The mass matrix can be diagonalized with the help of a unitary transformation $\mathbf{U}_{\tilde{q}}$,

$$\mathbf{D}_{\tilde{q}} = \mathbf{U}_{\tilde{q}}\mathbf{M}_{\tilde{q}}\mathbf{U}_{\tilde{q}}^\dagger = \begin{pmatrix} m_{\tilde{q}_1}^2 & 0 \\ 0 & m_{\tilde{q}_2}^2 \end{pmatrix}, \qquad \mathbf{U}_{\tilde{q}} = \begin{pmatrix} U_{\tilde{q}_{11}} & U_{\tilde{q}_{12}} \\ U_{\tilde{q}_{21}} & U_{\tilde{q}_{22}} \end{pmatrix}. \quad (6)$$

The scalar quark masses, $m_{\tilde{q}_1}$ and $m_{\tilde{q}_2}$, will always be mass ordered, i.e. $m_{\tilde{q}_1} \leq m_{\tilde{q}_2}$:

$$m^2_{\tilde{q}_{1,2}} = \frac{1}{2}(M^2_{\tilde{Q}_L} + M^2_{\tilde{q}_R}) + m^2_q + \frac{1}{2}T^3_q M^2_Z c_{2\beta} \mp \frac{1}{2} \times \sqrt{[M^2_{\tilde{Q}_L} - M^2_{\tilde{q}_R} + M^2_Z c_{2\beta}(T^3_q - 2Q_q s^2_w)]^2 + 4m^2_q |X_q|^2}. \quad (7)$$

The parameter renormalization can be performed as follows:

$$\mathbf{M}_{\tilde{q}} \to \mathbf{M}_{\tilde{q}} + \delta\mathbf{M}_{\tilde{q}}, \quad (8)$$

which means that the parameters in the mass matrix $\mathbf{M}_{\tilde{q}}$ are replaced by the renormalized parameters and a counterterm. After the expansion $\delta\mathbf{M}_{\tilde{q}}$ contains the counterterm part,

$$\delta\mathbf{M}_{\tilde{q}_{11}} = \delta M^2_{\tilde{Q}_L} + 2m_q\delta m_q - M^2_Z c_{2\beta} Q_q \delta s^2_w + (T^3_q - Q_q s^2_w)(c_{2\beta}\delta M^2_Z + M^2_Z \delta c_{2\beta}), \quad (9)$$

$$\delta\mathbf{M}_{\tilde{q}_{12}} = (A^*_q - \mu\kappa)\delta m_q + m_q(\delta A^*_q - \mu\delta\kappa - \kappa\delta\mu), \quad (10)$$

$$\delta\mathbf{M}_{\tilde{q}_{21}} = \delta\mathbf{M}^*_{\tilde{q}_{12}}, \quad (11)$$

$$\delta\mathbf{M}_{\tilde{q}_{22}} = \delta M^2_{\tilde{q}_R} + 2m_q\delta m_q + M^2_Z c_{2\beta} Q_q \delta s^2_w + Q_q s^2_w (c_{2\beta}\delta M^2_Z + M^2_Z \delta c_{2\beta}) \quad (12)$$

with κ given in Eq. (5).

Another possibility for the parameter renormalization is to start out with the physical parameters which corresponds to the replacement:

$$\mathbf{U}_{\tilde{q}}\mathbf{M}_{\tilde{q}}\mathbf{U}^\dagger_{\tilde{q}} \to \mathbf{U}_{\tilde{q}}\mathbf{M}_{\tilde{q}}\mathbf{U}^\dagger_{\tilde{q}} + \mathbf{U}_{\tilde{q}}\delta\mathbf{M}_{\tilde{q}}\mathbf{U}^\dagger_{\tilde{q}} = \begin{pmatrix} m^2_{\tilde{q}_1} & Y_q \\ Y^*_q & m^2_{\tilde{q}_2} \end{pmatrix} + \begin{pmatrix} \delta m^2_{\tilde{q}_1} & \delta Y_q \\ \delta Y^*_q & \delta m^2_{\tilde{q}_2} \end{pmatrix}, \quad (13)$$

where $\delta m^2_{\tilde{q}_1}$ and $\delta m^2_{\tilde{q}_2}$ are the counterterms of the squark masses squared. δY_q is the counterterm[1] to the squark mixing parameter Y_q [which vanishes at tree level, $Y_q = 0$, and corresponds to the off-diagonal entries in $\mathbf{D}_{\tilde{q}} = \mathbf{U}_{\tilde{q}}\mathbf{M}_{\tilde{q}}\mathbf{U}^\dagger_{\tilde{q}}$, see Eq. (6)]. Using Eq. (13) one can express $\delta\mathbf{M}_{\tilde{q}}$ by the counterterms $\delta m^2_{\tilde{q}_1}$, $\delta m^2_{\tilde{q}_2}$ and δY_q. Especially for $\delta\mathbf{M}_{\tilde{q}_{12}}$ one yields

$$\delta\mathbf{M}_{\tilde{q}_{12}} = U^*_{\tilde{q}_{11}}U_{\tilde{q}_{12}}(\delta m^2_{\tilde{q}_1} - \delta m^2_{\tilde{q}_2}) + U^*_{\tilde{q}_{11}}U_{\tilde{q}_{22}}\delta Y_q + U_{\tilde{q}_{12}}U^*_{\tilde{q}_{21}}\delta Y^*_q. \quad (14)$$

In the following the relation given by Eq. (10) and (14) will be used to express either δY_q, δA_q or δm_q by the other counterterms.

[1]The unitary matrix $\mathbf{U}_{\tilde{q}}$ can be expressed by a mixing angle $\theta_{\tilde{q}}$ and a corresponding phase $\varphi_{\tilde{q}}$. Then the counterterm δY_q can be related to the counterterms of the mixing angle and the phase (see Ref. [13]).

For the field renormalization the following procedure is applied:

$$\begin{pmatrix} \tilde{q}_1 \\ \tilde{q}_2 \end{pmatrix} \to \left(\mathbb{1} + \frac{1}{2}\delta\mathbf{Z}_{\tilde{q}}\right)\begin{pmatrix} \tilde{q}_1 \\ \tilde{q}_2 \end{pmatrix} \quad \text{with} \quad \delta\mathbf{Z}_{\tilde{q}} = \begin{pmatrix} \delta Z_{\tilde{q}_{11}} & \delta Z_{\tilde{q}_{12}} \\ \delta Z_{\tilde{q}_{21}} & \delta Z_{\tilde{q}_{22}} \end{pmatrix}. \quad (15)$$

This yields for the renormalized self-energies

$$\hat{\Sigma}_{\tilde{q}_{11}}(k^2) = \Sigma_{\tilde{q}_{11}}(k^2) + \tfrac{1}{2}(k^2 - m^2_{\tilde{q}_1}) \times (\delta Z_{\tilde{q}_{11}} + \delta Z^*_{\tilde{q}_{11}}) - \delta m^2_{\tilde{q}_1}, \quad (16)$$

$$\hat{\Sigma}_{\tilde{q}_{12}}(k^2) = \Sigma_{\tilde{q}_{12}}(k^2) + \tfrac{1}{2}(k^2 - m^2_{\tilde{q}_1})\delta Z_{\tilde{q}_{12}} + \tfrac{1}{2}(k^2 - m^2_{\tilde{q}_2})\delta Z^*_{\tilde{q}_{21}} - \delta Y_q, \quad (17)$$

$$\hat{\Sigma}_{\tilde{q}_{21}}(k^2) = \Sigma_{\tilde{q}_{21}}(k^2) + \tfrac{1}{2}(k^2 - m^2_{\tilde{q}_1})\delta Z^*_{\tilde{q}_{12}} + \tfrac{1}{2}(k^2 - m^2_{\tilde{q}_2})\delta Z_{\tilde{q}_{21}} - \delta Y^*_q, \quad (18)$$

$$\hat{\Sigma}_{\tilde{q}_{22}}(k^2) = \Sigma_{\tilde{q}_{22}}(k^2) + \tfrac{1}{2}(k^2 - m^2_{\tilde{q}_2}) \times (\delta Z_{\tilde{q}_{22}} + \delta Z^*_{\tilde{q}_{22}}) - \delta m^2_{\tilde{q}_2}. \quad (19)$$

In order to complete the quark/squark sector renormalization also for the corresponding quark (i.e. its mass, m_q, and the quark field, q) renormalization constants have to be introduced:

$$m_q \to m_q + \delta m_q, \quad (20)$$

$$\omega_\mp q \to (1 + \tfrac{1}{2}\delta Z^{L/R}_q)\omega_\mp q, \quad (21)$$

with δm_q being the quark mass counterterm and δZ^L_q and δZ^R_q being the Z factors of the left-handed and the right-handed component of the quark field q, respectively. $\omega_\mp = \frac{1}{2}(\mathbb{1} \mp \gamma_5)$ are the left- and right-handed projectors, respectively. Then the renormalized self-energy, $\hat{\Sigma}_q$, can be decomposed into left/right-handed and scalar left/right-handed parts, $\hat{\Sigma}^{L/R}_q$ and $\hat{\Sigma}^{SL/SR}_q$, respectively,

$$\hat{\Sigma}_q(k) = \not{k}\omega_-\hat{\Sigma}^L_q(k^2) + \not{k}\omega_+\hat{\Sigma}^R_q(k^2) + \omega_-\hat{\Sigma}^{SL}_q(k^2) + \omega_+\hat{\Sigma}^{SR}_q(k^2), \quad (22)$$

where the components are given by

$$\hat{\Sigma}^{L/R}_R(k^2) = \Sigma^{L/R}_q(k^2) + \tfrac{1}{2}(\delta Z^{L/R}_q + \delta Z^{L/R^*}_q), \quad (23)$$

$$\hat{\Sigma}^{SL}_q(k^2) = \Sigma^{SL}_q(k^2) - \frac{m_q}{2}(\delta Z^L_q + \delta Z^{R^*}_q) - \delta m_q, \quad (24)$$

$$\hat{\Sigma}^{SR}_q(k^2) = \Sigma^{SR}_q(k^2) - \frac{m_q}{2}(\delta Z^R_q + \delta Z^{L^*}_q) - \delta m_q. \quad (25)$$

Note that $\hat{\Sigma}^{SR}_q(k^2) = \hat{\Sigma}^{SL}_q(k^2)^*$ holds due to $\mathcal{CPT}$ invariance.

III. FIELD RENORMALIZATION OF THE QUARK/SQUARK SECTOR

We first discuss the field renormalization of the top- and bottom-quark/squark sector and turn to the parameter renormalization in the next Sec. IV.

The field renormalization, meaning the determination of the Z factors, is done within an on-shell scheme for squarks and quarks. We impose equivalent renormalization conditions for the top as well as for the bottom-quark/squark sector:

(a) The diagonal Z factors of the squark fields are determined such that the real part of the residua of propagators is set to unity,

$$\widetilde{\mathrm{Re}}\,\frac{\partial \hat{\Sigma}_{\tilde{q}_{ii}}(k^2)}{\partial k^2}\bigg|_{k^2=m^2_{\tilde{q}_i}} = 0 \qquad (i=1,2). \tag{26}$$

This condition fixes the real parts of the diagonal Z factors to

$$\mathrm{Re}\,\delta Z_{\tilde{q}_{ii}} = -\widetilde{\mathrm{Re}}\,\frac{\partial \Sigma_{\tilde{q}_{ii}}(k^2)}{\partial k^2}\bigg|_{k^2=m^2_{\tilde{q}_i}} \qquad (i=1,2). \tag{27}$$

$\widetilde{\mathrm{Re}}$ above denotes the real part with respect to contributions from the loop integral, but leaves the complex couplings unaffected.

The imaginary parts of the diagonal Z factors are so far undetermined and are set to zero,

$$\mathrm{Im}\,\delta Z_{\tilde{q}_{ii}} = 0 \qquad (i=1,2). \tag{28}$$

This is possible since they do not contain divergences.

(b) For the nondiagonal Z factors of the squark fields we impose the condition that for on-shell squarks no transition from one squark to the other occurs,

$$\widetilde{\mathrm{Re}}\hat{\Sigma}_{\tilde{q}_{12}}(m^2_{\tilde{q}_1}) = 0, \tag{29}$$

$$\widetilde{\mathrm{Re}}\hat{\Sigma}_{\tilde{q}_{12}}(m^2_{\tilde{q}_2}) = 0. \tag{30}$$

This yields

$$\begin{aligned}\delta Z_{\tilde{q}_{12}} &= +2\frac{\widetilde{\mathrm{Re}}\Sigma_{\tilde{q}_{12}}(m^2_{\tilde{q}_2}) - \delta Y_q}{(m^2_{\tilde{q}_1} - m^2_{\tilde{q}_2})},\\ \delta Z_{\tilde{q}_{21}} &= -2\frac{\widetilde{\mathrm{Re}}\Sigma_{\tilde{q}_{21}}(m^2_{\tilde{q}_1}) - \delta Y^*_q}{(m^2_{\tilde{q}_1} - m^2_{\tilde{q}_2})}.\end{aligned} \tag{31}$$

The counterterm δY_q is determined in the corresponding parameter renormalization scheme. This means the nondiagonal Z factors of the squark fields do also depend on the choice of the parameter renormalization scheme.

(c) The quark fields are also defined via an on-shell condition. We impose

$$\begin{aligned}\lim_{k^2\to m_q^2}\frac{\not{k}+m_q}{k^2-m_q^2}\,\widetilde{\mathrm{Re}}\hat{\Sigma}_q(k)u(k) = 0,\\ \lim_{k^2\to m_q^2}\bar{u}(k)\widetilde{\mathrm{Re}}\hat{\Sigma}_q(k)\frac{\not{k}+m_q}{k^2-m_q^2} = 0,\end{aligned} \tag{32}$$

where $u(k)$, $\bar{u}(k)$ are the spinors of the external fields. This yields

$$\begin{aligned}\mathrm{Re}\,\delta Z_q^{L/R} = -\widetilde{\mathrm{Re}}\{&\Sigma_q^{L/R}(m_q^2) + m_q^2[\Sigma_q^{L'}(m_q^2)\\ &+ \Sigma_q^{R'}(m_q^2)] + m_q[\Sigma_q^{SL'}(m_q^2)\\ &+ \Sigma_q^{SR'}(m_q^2)]\},\end{aligned} \tag{33}$$

$$\begin{aligned}m_q(\mathrm{Im}\delta Z_q^L - \mathrm{Im}\delta Z_q^R) &= i\,\widetilde{\mathrm{Re}}\{\Sigma_q^{SR}(m_q^2) - \Sigma_q^{SL}(m_q^2)\}\\ &= 2\,\mathrm{Im}\{\widetilde{\mathrm{Re}}\Sigma_q^{SL}(m_q^2)\},\end{aligned} \tag{34}$$

with $\Sigma'(k^2) \equiv \frac{\partial\Sigma(k^2)}{\partial k^2}$. Choosing also $\mathrm{Im}\delta Z_q^L = -\mathrm{Im}\delta Z_q^R$, the imaginary parts of the Z factors can be expressed as

$$\begin{aligned}\mathrm{Im}\delta Z_q^{L/R} &= \pm\frac{i}{2m_q}\,\widetilde{\mathrm{Re}}\{\Sigma_q^{SR}(m_q^2) - \Sigma_q^{SL}(m_q^2)\}\\ &= \pm\frac{1}{m_q}\,\mathrm{Im}\{\widetilde{\mathrm{Re}}\Sigma_q^{SL}(m_q^2)\}.\end{aligned} \tag{35}$$

Note that the renormalization condition Eq. (32) can only be fully satisfied if the corresponding quark mass is defined as on-shell, too.

The Z factors of the quark fields are not needed for the calculation of the considered decay modes of the scalar top quarks (see, however, Ref. [26]).

IV. PARAMETER RENORMALIZATION OF THE TOP- AND BOTTOM-QUARK/SQUARK SECTOR

Within the top- and bottom-quark/squark sector nine real parameters are defined: The real soft SUSY-breaking parameters $M^2_{\tilde{Q}_L}$, $M^2_{\tilde{t}_R}$ and $M^2_{\tilde{b}_R}$, the complex trilinear couplings A_t and A_b and the top- and bottom-Yukawa couplings y_t and y_b which both can be chosen to be real. (μ and $\tan\beta$ as well as the gauge boson masses and the weak mixing angle are determined within other sectors, see the beginning of Sec. II). Note that the soft SUSY-breaking parameter $M^2_{\tilde{Q}_L}$ is the same in the top as well as in the bottom squark sector due to the $SU(2)_L$ invariance of the left-handed fields. As in Refs. [9,13], instead of choosing the five quantities $M^2_{\tilde{Q}_L}, M^2_{\tilde{t}_R}, M^2_{\tilde{b}_R}$ and y_t, y_b the squark masses $m^2_{\tilde{t}_1}, m^2_{\tilde{t}_2}, m^2_{\tilde{b}_2}$ as well as the top- and bottom-quark masses m_t, m_b were taken as independent parameters.

If a regularization scheme is applied which does not break the symmetries of the model, it is sufficient to use

counterterms which respects the underlying symmetries. Such counterterms are generated by multiplicative renormalization of parameters and fields of the MSSM. The parameter counterterms can be fixed by as many renormalization conditions as independent parameters exist [29]. Concerning the top-and bottom-quark/squark sector we have to set nine renormalization conditions to define all independent parameters.

For the renormalization of the top-quark/squark sector we follow Refs. [9,13] but we also include electroweak contributions.

We impose five renormalization conditions, (A)–(E), to fix the parameters of the top-quark/squark sector:

(A) The top-quark mass is determined via an on-shell condition, yielding the one-loop counterterm δm_t:

$$\delta m_t = \tfrac{1}{2}\widetilde{\mathrm{Re}}\{m_t[\Sigma_t^L(m_t^2) + \Sigma_t^R(m_t^2)] + [\Sigma_t^{SL}(m_t^2) + \Sigma_t^{SR}(m_t^2)]\}. \quad (36)$$

(B), (C) The two top-squark masses are also defined on shell, yielding the real counterterms

$$\delta m^2_{\tilde{t}_i} = \widetilde{\mathrm{Re}}\Sigma_{\tilde{t}_{ii}}(m^2_{\tilde{t}_i}) \qquad (i = 1, 2). \quad (37)$$

(D), (E) Finally, the nondiagonal entry in the matrix of Eq. (13) is fixed as

$$\delta Y_t = \tfrac{1}{2}\widetilde{\mathrm{Re}}\{\Sigma_{\tilde{t}_{12}}(m^2_{\tilde{t}_1}) + \Sigma_{\tilde{t}_{12}}(m^2_{\tilde{t}_2})\}, \quad (38)$$

which corresponds to two separate conditions as δY_t is complex.

The counterterm of the trilinear coupling δA_t is then given via the relation of Eqs. (10) and (14) as

$$\delta A_t = \frac{1}{m_t}[U_{\tilde{t}_{11}} U^*_{\tilde{t}_{12}}(\delta m^2_{\tilde{t}_1} - \delta m^2_{\tilde{t}_2}) + U_{\tilde{t}_{11}} U^*_{\tilde{t}_{22}} \delta Y_t^* + U^*_{\tilde{t}_{12}} U_{\tilde{t}_{21}} \delta Y_t - (A_t - \mu^* \cot\beta)\delta m_t] + (\delta\mu^* \cot\beta - \mu^* \cot^2\beta \delta\tan\beta). \quad (39)$$

The definition of $\delta\tan\beta$ and $\delta\mu$ is indicated in Sec. II.

For the bottom-quark/squark sector we are left with four independent parameters which are not defined yet. We choose the following four renormalization conditions, (i)–(iv):

(i) The $\tilde{b}_2$ mass is defined on shell:

$$\delta m^2_{\tilde{b}_2} = \widetilde{\mathrm{Re}}\Sigma_{\tilde{b}_{22}}(m^2_{\tilde{b}_2}). \quad (40)$$

(ii)–(iv) These three renormalization conditions are chosen according to the different renormalization conditions listed in Table I and to the corresponding Secs. IV A, IV B, IV C, IV D, IV E, and IV F. They yield the counterterms δm_b, δA_b and δY_b where only three of these five real counterterms are independent (counting each of the complex counterterms, δA_b and δY_b, as two real counterterms). The two dependent counterterms can be expressed as a combination of the other ones.

Applying these renormalization conditions fixes the counterterms generated by multiplicative renormalization which fulfill the symmetry relations [29].

While the $\tilde{b}_2$ mass is defined on shell, the $\tilde{b}_1$ mass receives a shift due to the radiative corrections:

$$m^2_{\tilde{b}_{1,\mathrm{OS}}} = m^2_{\tilde{b}_1} + (\delta m^2_{\tilde{b}_1} - \widetilde{\mathrm{Re}}\Sigma_{\tilde{b}_{11}}(m^2_{\tilde{b}_1})). \quad (41)$$

The term in parentheses is the shift from $m^2_{\tilde{b}_1}$ to the on-shell mass squared. The value of $m^2_{\tilde{b}_1}$ is derived from the diagonalization of the sbottom mass matrix, see Eq. (6), and $\delta m^2_{\tilde{b}_1}$ is defined as a dependent quantity [10,30]. $m^2_{\tilde{b}_{1,\mathrm{OS}}}$ is the on-shell $\tilde{b}_1$ mass squared. In Ref. [30] the size of the shift was analyzed while in Ref. [10] bottom squarks appeared only as ''internal'' particles, i.e. as particles inside the loop diagrams. Concerning the scalar top-quark decay, Eqs. (1) and (2), we are now dealing with scalar bottom quarks as ''external'' particles, which are defined as incoming or outgoing particles. These external particles should fulfill on-shell properties. At this point there are two options to proceed:

($\mathcal{O}1$) The first option is to use different mass values, $m_{\tilde{b}_1}$ and $m_{\tilde{b}_{1,\mathrm{OS}}}$, for the internal and the external particles,

TABLE I. Summary of the six renormalization schemes for the $b/\tilde{b}$ sector investigated below. Blank entries indicate dependent quantities. ReY_b denotes that only the real part of Y_b is renormalized on shell, while the imaginary part is a dependent parameter. The rightmost columns indicates the section that contains the detailed description of the respective renormalization and the abbreviated notation used in our analysis.

Scheme	$m_{\tilde{b}_{1,2}}$	m_b	A_b	Y_b	Sec.	Name
Analogous to the $t/\tilde{t}$ sector: ''OS''	OS	OS		OS	4.1	RS1
''m_b, $A_b\overline{\mathrm{DR}}$''	OS	$\overline{\mathrm{DR}}$	$\overline{\mathrm{DR}}$		4.2	RS2
''m_b, $Y_b\overline{\mathrm{DR}}$''	OS	$\overline{\mathrm{DR}}$		$\overline{\mathrm{DR}}$	4.3	RS3
''$m_b\overline{\mathrm{DR}}$, Y_b OS''	OS	$\overline{\mathrm{DR}}$		OS	4.4	RS4
''$A_b\overline{\mathrm{DR}}$, Re$Y_b$ OS''	OS		$\overline{\mathrm{DR}}$	ReY_b: OS	4.5	RS5
''A_b vertex, ReY_b OS''	OS		vertex	ReY_b: OS	4.6	RS6

respectively, which can cause problems for charged particles as, for instance, scalar bottom quarks (see below).

($\mathcal{O}2$) The second option is to impose a further renormalization condition which ensures that the $\tilde{b}_1$ mass is on shell:

$$\delta m^2_{\tilde{b}_1} = \widetilde{\mathrm{Re}}\Sigma_{\tilde{b}_{11}}(m^2_{\tilde{b}_1}). \tag{42}$$

In this case the input has to be chosen such that the symmetry relations are fulfilled at the one-loop level.

As mentioned above, the option ($\mathcal{O}1$) leads to a problem. The IR divergences originating from the loop diagrams involve the "inner" (i.e. tree-level) mass $m_{\tilde{b}_1}$. These have to cancel with the real Bremsstrahlung IR divergences, which are evaluated with the help of the external (i.e. one-loop on-shell) mass $m_{\tilde{b}_{1,\mathrm{OS}}}$, which is inserted into the tree-level diagram (the result can, as usual, be expressed with the help of the soft Bremsstrahlung (SB) factor δ_{SB}: $\mathcal{M}_{\mathrm{tree}} \times \delta_{\mathrm{SB}}$, see Ref. [28]). Because of the two different sets of masses the IR divergences do not cancel. One way out would be the use of tree-level masses in all diagrams contributing to the part $2\,\mathrm{Re}\{\mathcal{M}^*_{\mathrm{tree}}\mathcal{M}_{\mathrm{loop}}\}$, i.e. in all loop diagrams and in the hard and soft Bremsstrahlung diagrams. However, this would lead to inconsistencies in the evaluation of the complete loop corrected amplitude squared $\propto (|\mathcal{M}_{\mathrm{tree}}|^2 + 2\,\mathrm{Re}\{\mathcal{M}^*_{\mathrm{tree}}\mathcal{M}_{\mathrm{loop}}\})$ due to the different masses entering the phase space evaluation. A consistent phase space integration requires the use of the same external masses for all outgoing particles in all parts of the calculation.

To circumvent the problem of the noncancellation of IR divergences we choose the option ($\mathcal{O}2$) and impose the further renormalization condition Eq. (42). This requires to choose an input that restores the symmetries. Relating $(\mathbf{M}_{\tilde{q}})_{11}$ of Eq. (4) and $(\mathbf{U}_{\tilde{\mathbf{q}}}{}^{\dagger}\mathbf{D}_{\tilde{q}}\mathbf{U}_{\tilde{\mathbf{q}}})_{11}$ with $\mathbf{D}_{\tilde{q}}$ of Eq. (6) yields an expression for the soft SUSY-breaking parameter $M^2_{\tilde{Q}_L}$ (depending on the squark flavor),

$$\begin{aligned} M^2_{\tilde{Q}_L}(\tilde{q}) = {} & |U_{\tilde{q}_{11}}|^2 m^2_{\tilde{q}_1} + |U_{\tilde{q}_{12}}|^2 m^2_{\tilde{q}_2} \\ & - M^2_Z c_{2\beta}(T^3_q - Q_q s^2_{\mathrm{w}}) - m^2_q \end{aligned} \tag{43}$$

with $\tilde{q} = \{\tilde{t}, \tilde{b}\}$. Requiring the $SU(2)_L$ relation to be valid at the one-loop level induces the following shift in $M^2_{\tilde{Q}_L}$ (see also Refs. [2,3,31]):

$$M^2_{\tilde{Q}_L}(\tilde{b}) = M^2_{\tilde{Q}_L}(\tilde{t}) + \delta M^2_{\tilde{Q}_L}(\tilde{t}) - \delta M^2_{\tilde{Q}_L}(\tilde{b}), \tag{44}$$

with

$$\begin{aligned} \delta M^2_{\tilde{Q}_L}(\tilde{q}) = {} & |U_{\tilde{q}_{11}}|^2 \delta m^2_{\tilde{q}_1} + |U_{\tilde{q}_{12}}|^2 \delta m^2_{\tilde{q}_2} - U_{\tilde{q}_{22}} U^*_{\tilde{q}_{12}} \delta Y_q \\ & - U_{\tilde{q}_{12}} U^*_{\tilde{q}_{22}} \delta Y^*_q - 2 m_q \delta m_q + M^2_Z c_{2\beta} Q_q \delta s^2_{\mathrm{w}} \\ & - (T^3_q - Q_q s^2_{\mathrm{w}})(c_{2\beta}\delta M^2_Z + M^2_Z \delta c_{2\beta}). \end{aligned} \tag{45}$$

In other words, everywhere in the calculation the masses and mixing matrix elements coming from the diagonalization of the bottom squark mass matrix, see Eq. (6), are used with $M^2_{\tilde{Q}_L}(\tilde{b})$ including the above shift as in Eq. (44). In this way the problems concerning UV- and IR-finiteness are avoided. (An exception is the field renormalization of the W-boson field: In the corresponding self-energies the $SU(2)_L$ relation is needed at tree level to ensure UV finiteness. In this case, tree-level bottom squark masses are used.)

The various renormalization schemes, following the general choice ($\mathcal{O}2$), are summarized in Table I and outlined in detail in the following subsections.

Comparing with the literature, several of the renormalization schemes (or variants of them) have been used to calculate higher-order corrections to squark or Higgs decays. The older calculations of the loop corrections have all been performed in the rMSSM.

(i) A renormalization scheme employing an "OS" renormalization for m_b and Y_b was used in Refs. [3,5] for the calculation of stop and sbottom decays. (The calculation of Ref. [3] is also implemented in Ref. [4].) In order to check our implementation given in Sec. IVA we calculated the decay $\tilde{b}_{1,2} \to \tilde{t}_1 H^-$ (see Sec. VA for our setup) and found good agreement with Ref. [3].

(ii) A renormalization scheme similar to the real version of RS2, i.e. "m_b, A_b $\overline{\mathrm{DR}}$" has been employed in Ref. [7] for the calculation of Higgs decays to scalar fermions. In the scalar top and the Higgs sector they apply an on-shell scheme (partially based on Refs. [32,33]), which differs in some points from our renormalization scheme.

(iii) An on-shell scheme was also used in Ref. [34] (based on Refs. [32,35]) to evaluate the decay $\tilde{f} \to \tilde{f}' V$ ($V = W^{\pm}, Z$).

(iv) In Ref. [36], as a starting point, an on-shell renormalization scheme was used for the calculation of the electroweak corrections to $\Gamma(\tilde{t}_2 \to \tilde{t}_1 \phi)$, ($\phi = h, H, A$). To improve the calculation, the parameters m_b, m_t, A_t and A_b have also been used as running parameters.

(v) Other "early" papers considered QCD corrections to various scalar quark decays [37–39]. They mostly employed an on-shell scheme for the quark/squark masses and the squark mixing angle $\theta_{\tilde{q}}$, where the counterterm to the mixing angle is $\delta\theta_{\tilde{q}} \propto \delta Y_q$.

(vi) The renormalization scheme "A_b vertex, $\mathrm{Re}Y_b$ OS" is the complex version of the renormalization used in Refs. [10,11] for the $\mathcal{O}(\alpha_b \alpha_s)$ corrections to the neutral Higgs boson self-energies and thus to the lightest MSSM Higgs boson mass, M_h.

In the following subsections we define in detail the various renormalization schemes. As explained before and indicated in Table I the two bottom squark masses

are renormalized on shell in all the schemes, as in Eqs. (40) and (42), and taking into account the shift of $M^2_{\tilde{Q}_L}(\tilde{b})$ in Eq. (44). Within the subsections only the remaining conditions and renormalization constants are defined explicitly (where $\delta\mu$ and $\delta\tan\beta$ are defined within the chargino/neutralino sector and the Higgs sector, respectively, in all the different renormalization schemes and are not discussed any further).

A. On-shell (RS1)

This renormalization scheme is analogous to the OS scheme employed for the top-quark/squark sector.

(ii) The bottom-quark mass is defined OS, yielding the one-loop counterterm δm_b:

$$\delta m_b = \tfrac{1}{2}\widetilde{\mathrm{Re}}\{m_b[\Sigma_b^L(m_b^2) + \Sigma_b^R(m_b^2)] + [\Sigma_b^{SL}(m_b^2) + \Sigma_b^{SL}(m_b^2)]\}. \quad (46)$$

(iii), (iv) We choose an OS renormalization condition for the nondiagonal entry in the matrix of Eq. (13), analogous to the one applied in the top-quark/squark sector, setting

$$\delta Y_b = \tfrac{1}{2}\widetilde{\mathrm{Re}}\{\Sigma_{\tilde{b}_{12}}(m^2_{\tilde{b}_1}) + \Sigma_{\tilde{b}_{12}}(m^2_{\tilde{b}_2})\}. \quad (47)$$

The conditions (i)–(iv) fix all independent parameters and their respective counterterms. Analogous to the calculation of the counterterm of the trilinear coupling A_t, relating Eq. (10) and (14) yields the following condition for δA_b,

$$\delta A_b = \frac{1}{m_b}[U_{\tilde{b}_{11}}U^*_{\tilde{b}_{12}}(\delta m^2_{\tilde{b}_1} - \delta m^2_{\tilde{b}_2}) + U_{\tilde{b}_{11}}U^*_{\tilde{b}_{22}}\delta Y_b^* + U^*_{\tilde{b}_{12}}U_{\tilde{b}_{21}}\delta Y_b - (A_b - \mu^*\tan\beta)\delta m_b] + (\delta\mu^*\tan\beta + \mu^*\delta\tan\beta), \quad (48)$$

with $\delta m^2_{\tilde{b}_1}$ and $\delta m^2_{\tilde{b}_2}$ given in Eqs. (42) and (40), respectively.

B. m_b $\overline{\mathrm{DR}}$ and A_b $\overline{\mathrm{DR}}$ (RS2)

(ii) The bottom-quark mass is defined $\overline{\mathrm{DR}}$, yielding the one-loop counterterm δm_b:

$$\delta m_b = \tfrac{1}{2}\widetilde{\mathrm{Re}}\{m_b[\Sigma_b^L(m_b^2) + \Sigma_b^R(m_b^2)]_{\mathrm{div}} + [\Sigma_b^{SL}(m_b^2) + \Sigma_b^{SR}(m_b^2)]_{\mathrm{div}}\}. \quad (49)$$

The $|_{\mathrm{div}}$ terms are the ones proportional to $\Delta = 2/\varepsilon - \gamma_E + \log(4\pi)$, when using dimensional regularization/reduction in $D = 4 - \varepsilon$ dimensions; γ_E is the Euler constant.

(iii), (iv) The complex parameter A_b is renormalized $\overline{\mathrm{DR}}$,

$$\delta A_b = \frac{1}{m_b}[U_{\tilde{b}_{11}}U^*_{\tilde{b}_{12}}(\widetilde{\mathrm{Re}}\Sigma_{\tilde{b}_{11}}(m^2_{\tilde{b}_1})|_{\mathrm{div}} - \widetilde{\mathrm{Re}}\Sigma_{\tilde{b}_{22}}(m^2_{\tilde{b}_2})|_{\mathrm{div}}) + \frac{1}{2}U^*_{\tilde{b}_{12}}U_{\tilde{b}_{21}}(\widetilde{\mathrm{Re}}\Sigma_{\tilde{b}_{12}}(m^2_{\tilde{b}_1})|_{\mathrm{div}} + \widetilde{\mathrm{Re}}\Sigma_{\tilde{b}_{12}}(m^2_{\tilde{b}_2})|_{\mathrm{div}}) + \frac{1}{2}U_{\tilde{b}_{11}}U^*_{\tilde{b}_{22}}(\widetilde{\mathrm{Re}}\Sigma_{\tilde{b}_{12}}(m^2_{\tilde{b}_1})|_{\mathrm{div}} + \widetilde{\mathrm{Re}}\Sigma_{\tilde{b}_{12}}(m^2_{\tilde{b}_2})|_{\mathrm{div}})^* - \frac{1}{2}(A_b - \mu^*\tan\beta)\widetilde{\mathrm{Re}}\{m_b[\Sigma_b^L(m_b^2) + \Sigma_b^R(m_b^2)]_{\mathrm{div}} + [\Sigma_b^{SL}(m_b^2) + \Sigma_b^{SR}(m_b^2)]_{\mathrm{div}}\}] + \delta\mu^*|_{\mathrm{div}}\tan\beta + \mu^*\delta\tan\beta. \quad (50)$$

All independent parameters are defined by the conditions (i)–(iv) and the corresponding counterterms are determined. Solving Eqs. (10) and (14) for δY_b yields

$$\delta Y_b = \frac{1}{|U_{\tilde{b}_{11}}|^2 - |U_{\tilde{b}_{12}}|^2}[U_{\tilde{b}_{11}}U^*_{\tilde{b}_{21}}(\delta m^2_{\tilde{b}_1} - \delta m^2_{\tilde{b}_2}) + m_b(U_{\tilde{b}_{11}}U^*_{\tilde{b}_{22}}(\delta A_b^* - \mu\delta\tan\beta - \tan\beta\delta\mu) - U_{\tilde{b}_{12}}U^*_{\tilde{b}_{21}}(\delta A_b - \mu^*\delta\tan\beta - \tan\beta\delta\mu^*)) + (U_{\tilde{b}_{11}}U^*_{\tilde{b}_{22}}(A_b^* - \mu\tan\beta) - U_{\tilde{b}_{12}}U^*_{\tilde{b}_{21}}(A_b - \mu^*\tan\beta))\delta m_b], \quad (51)$$

where $\delta m^2_{\tilde{b}_1}$ and $\delta m^2_{\tilde{b}_2}$ are given in Eqs. (42) and (40), respectively.

C. m_b $\overline{\mathrm{DR}}$ and Y_b $\overline{\mathrm{DR}}$ (RS3)

(ii) The bottom-quark mass is defined $\overline{\mathrm{DR}}$, yielding the one-loop counterterm δm_b:

$$\delta m_b = \tfrac{1}{2}\widetilde{\mathrm{Re}}\{m_b[\Sigma_b^L(m_b^2) + \Sigma_b^R(m_b^2)]_{\mathrm{div}} + [\Sigma_b^{SL}(m_b^2) + \Sigma_b^{SR}(m_b^2)]_{\mathrm{div}}\}. \quad (52)$$

(iii), (iv) The complex counterterm δY_b is determined via a $\overline{\mathrm{DR}}$ renormalization condition, setting

$$\delta Y_b = \tfrac{1}{2}\widetilde{\mathrm{Re}}\{\Sigma_{\tilde{b}_{12}}(m^2_{\tilde{b}_1})|_{\mathrm{div}} + \Sigma_{\tilde{b}_{12}}(m^2_{\tilde{b}_2})|_{\mathrm{div}}\}. \quad (53)$$

As in Sec. IV A, the renormalization conditions (ii), (iii) and (iv) fix the counterterms δm_b and δY_b, respectively. Together with the renormalization conditions for $\delta m^2_{\tilde{b}_1}$ and $\delta m^2_{\tilde{b}_2}$ [see Eq. (42) and (40), respectively], δA_b is given by the linear combination of these counterterms as

$$\delta A_b = \frac{1}{m_b}[U_{\tilde{b}_{11}}U^*_{\tilde{b}_{12}}(\delta m^2_{\tilde{b}_1} - \delta m^2_{\tilde{b}_2}) + U_{\tilde{b}_{11}}U^*_{\tilde{b}_{22}}\delta Y_b^* + U^*_{\tilde{b}_{12}}U_{\tilde{b}_{21}}\delta Y_b - (A_b - \mu^*\tan\beta)\delta m_b] + (\delta\mu^*\tan\beta + \mu^*\delta\tan\beta), \quad (54)$$

which, of course, shows the same analytical dependence of the independent counterterms as δA_b in Eq. (48) in Sec. IV A.

D. m_b $\overline{\rm DR}$ and Y_b on-shell (RS4)

(ii) The bottom-quark mass is defined $\overline{\rm DR}$, yielding the one-loop counterterm δm_b:

$$\delta m_b = \tfrac{1}{2}\widetilde{\rm Re}\{m_b[\Sigma_b^L(m_b^2) + \Sigma_b^R(m_b^2)]_{\rm div} + [\Sigma_b^{SL}(m_b^2) + \Sigma_b^{SR}(m_b^2)]_{\rm div}\}. \quad (55)$$

(iii), (iv) The complex counterterm δY_b is fixed by an on-shell renormalization condition, as in Sec. IV A,

$$\delta Y_b = \tfrac{1}{2}\widetilde{\rm Re}\{\Sigma_{\tilde b_{12}}(m_{\tilde b_1}^2) + \Sigma_{\tilde b_{12}}(m_{\tilde b_2}^2)\}. \quad (56)$$

As in Sec. IV A and in Sec. IV C, the renormalization conditions (i)–(iv) fix the counterterms $\delta m_{\tilde b_2}^2$, δm_b and δY_b. The further renormalization condition Eq. (42) determines the counterterm $\delta m_{\tilde b_1}^2$. Analogous to Sec. IV A and to Sec. IV C, δA_b can be expressed in terms of these counterterms,

$$\delta A_b = \frac{1}{m_b}[U_{\tilde b_{11}} U_{\tilde b_{12}}^*(\delta m_{\tilde b_1}^2 - \delta m_{\tilde b_2}^2) + U_{\tilde b_{11}} U_{\tilde b_{22}}^* \delta Y_b^* + U_{\tilde b_{12}}^* U_{\tilde b_{21}} \delta Y_b - (A_b - \mu^* \tan\beta)\delta m_b] + (\delta\mu^* \tan\beta + \mu^* \delta\tan\beta), \quad (57)$$

which, of course, has the same form as in Eqs. (48) and (54).

E. A_b $\overline{\rm DR}$ and ${\rm Re}\, b$ on-shell (RS5)

(ii) In the Secs. IV A, IV B, IV C, and IV D the second renormalization condition defines the bottom-quark mass. In this scheme, we choose an on-shell renormalization condition for the real part of the counterterm δY_b which determines ${\rm Re}\delta Y_b$ as follows:

$${\rm Re}\,\delta Y_b = \tfrac{1}{2}{\rm Re}\{\widetilde{\rm Re}\Sigma_{\tilde b_{12}}(m_{\tilde b_1}^2) + \widetilde{\rm Re}\Sigma_{\tilde b_{12}}(m_{\tilde b_2}^2)\}. \quad (58)$$

(iii), (iv) The complex A_b parameter is defined $\overline{\rm DR}$

$$\delta A_b = \frac{1}{m_b}[U_{\tilde b_{11}} U_{\tilde b_{12}}^*(\widetilde{\rm Re}\Sigma_{\tilde b_{11}}(m_{\tilde b_1}^2)|_{\rm div} - \widetilde{\rm Re}\Sigma_{\tilde b_{22}}(m_{\tilde b_2}^2)|_{\rm div}) + \tfrac{1}{2}U_{\tilde b_{12}}^* U_{\tilde b_{21}}(\widetilde{\rm Re}\Sigma_{\tilde b_{12}}(m_{\tilde b_1}^2)|_{\rm div} + \widetilde{\rm Re}\Sigma_{\tilde b_{12}}(m_{\tilde b_2}^2)|_{\rm div}) + \tfrac{1}{2}U_{\tilde b_{11}} U_{\tilde b_{22}}^*(\widetilde{\rm Re}\Sigma_{\tilde b_{12}}(m_{\tilde b_1}^2)|_{\rm div} + \widetilde{\rm Re}\Sigma_{\tilde b_{12}}(m_{\tilde b_2}^2)|_{\rm div})^* - \tfrac{1}{2}(A_b - \mu^* \tan\beta)\widetilde{\rm Re}\{m_b[\Sigma_b^L(m_b^2) + \Sigma_b^R(m_b^2)]_{\rm div} + [\Sigma_b^{SL}(m_b^2) + \Sigma_b^{SR}(m_b^2)]_{\rm div}\} + \delta\mu^*|_{\rm div}\tan\beta + \mu^*\delta\tan\beta. \quad (59)$$

With the conditions (i)–(iv) the independent counterterms $\delta m_{\tilde b_2}^2$, ${\rm Re}\delta Y_b$ and δA_b are determined, and $\delta m_{\tilde b_1}^2$ is given by Eq. (42). The missing counterterms δm_b and ${\rm Im}\delta Y_b$ can be expressed by the independent counterterms. Relating Eq. (10), here explicitly written as

$$(\delta \mathbf{M}_{\tilde b})_{12} = (A_b^* - \mu\tan\beta)\delta m_b + m_b(\delta A_b^* - \mu\delta\tan\beta - \delta\mu\tan\beta), \quad (60)$$

and Eq. (14), here with δY_b explicitly split into a real and an imaginary part

$$(\delta \mathbf{M}_{\tilde b})_{12} = U_{\tilde b_{11}}^* U_{\tilde b_{12}}(\delta m_{\tilde b_1}^2 - \delta m_{\tilde b_2}^2) + U_{\tilde b_{11}}^* U_{\tilde b_{22}}({\rm Re}\delta Y_b + i\,{\rm Im}\delta Y_b) + U_{\tilde b_{12}} U_{\tilde b_{21}}^*({\rm Re}\delta Y_b - i\,{\rm Im}\delta Y_b), \quad (61)$$

results in the two equations

$${\rm Re}\{A_b^* - \mu\tan\beta\}\delta m_b = -m_b\,{\rm Re}\delta A_b - {\rm Re}\delta S - {\rm Im}\{U_{\tilde b_{11}}^* U_{\tilde b_{22}} - U_{\tilde b_{12}} U_{\tilde b_{21}}^*\}{\rm Im}\delta Y_b, \quad (62)$$

$${\rm Im}\{A_b^* - \mu\tan\beta\}\delta m_b = +m_b\,{\rm Im}\delta A_b - {\rm Im}\delta S + {\rm Re}\{U_{\tilde b_{11}}^* U_{\tilde b_{22}} - U_{\tilde b_{12}} U_{\tilde b_{21}}^*\}{\rm Im}\delta Y_b \quad (63)$$

with

$$\delta S = -m_b(\mu\delta\tan\beta + \delta\mu\tan\beta) - U_{\tilde b_{11}}^* U_{\tilde b_{12}}(\delta m_{\tilde b_1}^2 - \delta m_{\tilde b_2}^2) - (U_{\tilde b_{11}}^* U_{\tilde b_{22}} + U_{\tilde b_{12}} U_{\tilde b_{21}}^*){\rm Re}\delta Y_b, \quad (64)$$

where $\delta m_{\tilde b_1}^2$ and $\delta m_{\tilde b_2}^2$ are given by Eq. (42) and (40).

The above two equations, (62) and (63), can be solved for ${\rm Im}\delta Y_b$ and δm_b, yielding

$$\delta m_b = \frac{b_r c_i - b_i c_r}{a_r b_i - a_i b_r}, \quad (65)$$

$${\rm Im}\,\delta Y_b = \frac{a_i c_r - a_r c_i}{a_r b_i - a_i b_r} \quad (66)$$

with

$$a_r = {\rm Re}\{A_b^* - \mu\tan\beta\}, \quad (67)$$

$$a_i = {\rm Im}\{A_b^* - \mu\tan\beta\}, \quad (68)$$

$$b_r = +{\rm Im}\{U_{\tilde b_{11}}^* U_{\tilde b_{22}} - U_{\tilde b_{12}} U_{\tilde b_{21}}^*\}, \quad (69)$$

$$b_i = -{\rm Re}\{U_{\tilde b_{11}}^* U_{\tilde b_{22}} - U_{\tilde b_{12}} U_{\tilde b_{21}}^*\}, \quad (70)$$

$$c_r = +m_b\,{\rm Re}\delta A_b + {\rm Re}\delta S, \quad (71)$$

$$c_i = -m_b\,{\rm Im}\delta A_b + {\rm Im}\delta S. \quad (72)$$

F. A_b via vertex and $\mathrm{Re}Y_b$ (RS6)

(ii) An on-shell renormalization condition is imposed for the real part of the counterterm δY_b which determines $\mathrm{Re}\delta Y_b$ as

$$\mathrm{Re}\,\delta Y_b = \tfrac{1}{2}\mathrm{Re}\{\widetilde{\mathrm{Re}}\Sigma_{\tilde{b}_{12}}(m^2_{\tilde{b}_1}) + \widetilde{\mathrm{Re}}\Sigma_{\tilde{b}_{12}}(m^2_{\tilde{b}_2})\}. \tag{73}$$

(iii), (iv) The renormalization conditions introduced here are analogous to the prescriptions used in Refs. [9–11], but extended to the complex MSSM. The complex parameter A_b is renormalized via the vertex $A\tilde{b}^\dagger_1\tilde{b}_2$, denoting the renormalized vertex as $\hat{\Lambda}(p^2_A, p^2_{\tilde{b}_1}, p^2_{\tilde{b}_2})$, see Fig. 1.

The tree-level vertex $A\tilde{b}^\dagger_1\tilde{b}_2$, denoted as $V_{A\tilde{b}^\dagger_1\tilde{b}_2}$, is given as

$$V_{A\tilde{b}^\dagger_1\tilde{b}_2} = \frac{iem_b}{2M_W s_\mathrm{w}\cos\beta}[U_{\tilde{b}_{11}}U^*_{\tilde{b}_{22}}(\mu\cos\beta_\mathrm{n} + A^*_b\sin\beta_\mathrm{n}) - U_{\tilde{b}_{12}}U^*_{\tilde{b}_{21}}(\mu^*\cos\beta_\mathrm{n} + A_b\sin\beta_\mathrm{n})], \tag{74}$$

where β_n is the mixing angle of the $\mathcal{CP}$-odd Higgs boson fields with $\beta_\mathrm{n} = \beta$ at tree level. Note that in our renormalization prescription we do not renormalize the mixing angles but only $\tan\beta$ appearing in the Lagrangian before the transformation of the $\mathcal{CP}$-odd Higgs boson fields into mass eigenstate fields is performed. The renormalized vertex reads,

$$\begin{aligned}\hat{\Lambda}(p^2_A, p^2_{\tilde{b}_1}, p^2_{\tilde{b}_2}) = {}& \Lambda(p^2_A, p^2_{\tilde{b}_1}, p^2_{\tilde{b}_2}) + \frac{iem_b}{2M_W s_\mathrm{w}}\Big\{\tan\beta[U_{\tilde{b}_{11}}U^*_{\tilde{b}_{22}}\delta A^*_b - U_{\tilde{b}_{12}}U^*_{\tilde{b}_{21}}\delta A_b] + [U_{\tilde{b}_{11}}U^*_{\tilde{b}_{22}}\delta\mu - U_{\tilde{b}_{12}}U^*_{\tilde{b}_{21}}\delta\mu^*] \\ & + [U_{\tilde{b}_{11}}U^*_{\tilde{b}_{22}}(\mu + \tan\beta A^*_b) - U_{\tilde{b}_{12}}U^*_{\tilde{b}_{21}}(\mu^* + \tan\beta A_b)] \\ & \times\left[\frac{\delta m_b}{m_b} + \frac{1}{2}(\delta\bar{Z}^*_{\tilde{b}_{11}} + \delta\bar{Z}_{\tilde{b}_{22}} + \delta Z_{AA}) + \sin\beta\cos\beta\,\delta\tan\beta\right] \\ & + [U_{\tilde{b}_{11}}U^*_{\tilde{b}_{22}}(\mu + \tan\beta A^*_b) - U_{\tilde{b}_{12}}U^*_{\tilde{b}_{21}}(\mu^* + \tan\beta A_b)]\left(\delta Z_e - \frac{\delta M^2_W}{2M^2_W} - \frac{\delta s_\mathrm{w}}{s_\mathrm{w}}\right) \\ & + i\,\mathrm{Im}\{U_{\tilde{b}_{11}}U^*_{\tilde{b}_{12}}(\mu + \tan\beta A^*_b)\}\delta Z_{\tilde{b}_{12}} + i\,\mathrm{Im}\{U_{\tilde{b}_{21}}U^*_{\tilde{b}_{22}}(\mu + \tan\beta A^*_b)\}\delta Z^*_{\tilde{b}_{21}} \\ & - \frac{1}{2}[U_{\tilde{b}_{11}}U^*_{\tilde{b}_{22}}(A^*_b - \mu\tan\beta) - U_{\tilde{b}_{12}}U^*_{\tilde{b}_{21}}(A_b - \mu^*\tan\beta)]\delta Z_{AG}\Big\}.\end{aligned} \tag{75}$$

The off-diagonal Z factors are determined according to Eq. (31),

$$\begin{aligned}\delta Z_{\tilde{b}_{12}} &= +2\frac{\widetilde{\mathrm{Re}}\Sigma_{\tilde{b}_{12}}(m^2_{\tilde{b}_2}) - \mathrm{Re}\delta Y_b - i\,\mathrm{Im}\delta Y_b}{(m^2_{\tilde{b}_1} - m^2_{\tilde{b}_2})} \\ &=: \delta Z^\mathrm{c}_{\tilde{b}_{12}} - \frac{2i\,\mathrm{Im}\delta Y_b}{m^2_{\tilde{b}_1} - m^2_{\tilde{b}_2}}, \\ \delta Z_{\tilde{b}_{21}} &= -2\frac{\widetilde{\mathrm{Re}}\Sigma_{\tilde{b}_{21}}(m^2_{\tilde{b}_1}) - \mathrm{Re}\delta Y_b + i\,\mathrm{Im}\delta Y_b}{(m^2_{\tilde{b}_1} - m^2_{\tilde{b}_2})} \\ &=: \delta Z^\mathrm{c}_{\tilde{b}_{21}} - \frac{2i\,\mathrm{Im}\delta Y_b}{m^2_{\tilde{b}_1} - m^2_{\tilde{b}_2}}.\end{aligned} \tag{76}$$

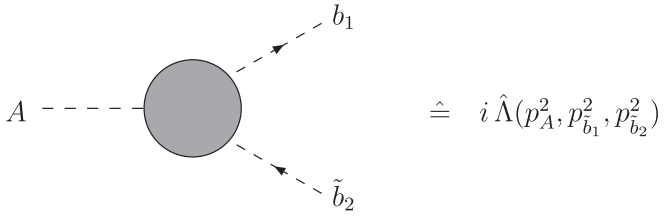

FIG. 1. The renormalized vertex $\hat{\Lambda}(p^2_A, p^2_{\tilde{b}_1}, p^2_{\tilde{b}_2})$.

Introducing appropriate abbreviations we get

$$\begin{aligned}\hat{\Lambda}(p^2_A, p^2_{\tilde{b}_1}, p^2_{\tilde{b}_2}) = {}& \Lambda(p^2_A, p^2_{\tilde{b}_1}, p^2_{\tilde{b}_2}) + \frac{ie}{2M_W s_\mathrm{w}} \\ & \times\{m_b\tan\beta(U_{\tilde{b}_{11}}U^*_{\tilde{b}_{22}}\delta A^*_b - U_{\tilde{b}_{12}}U^*_{\tilde{b}_{21}}\delta A_b) \\ & + \delta M + iU_Y\,\mathrm{Im}\delta Y_b + [U_{\tilde{b}_{11}}U^*_{\tilde{b}_{22}}(\mu + \tan\beta A^*_b) \\ & - U_{\tilde{b}_{12}}U^*_{\tilde{b}_{21}}(\mu^* + \tan\beta A_b)](\delta m_b + \delta Z_\mathrm{d})\} + \delta Z_\mathrm{o}\end{aligned} \tag{77}$$

with

$$\delta M = m_b[U_{\tilde{b}_{11}}U^*_{\tilde{b}_{22}}\delta\mu - U_{\tilde{b}_{12}}U^*_{\tilde{b}_{21}}\delta\mu^*], \tag{78}$$

$$U_Y = \frac{4im_b}{m^2_{\tilde{b}_1} - m^2_{\tilde{b}_2}}\,\mathrm{Im}\{U^*_{\tilde{b}_{11}}U_{\tilde{b}_{12}}(\mu^* + \tan\beta A_b)\}, \tag{79}$$

$$\delta Z_\mathrm{d} = m_b[\tfrac{1}{2}(\delta\bar{Z}^*_{\tilde{b}_{11}} + \delta\bar{Z}_{\tilde{b}_{22}} + \delta Z_{AA}) + \sin\beta\cos\beta\,\delta\tan\beta], \tag{80}$$

$$\delta Z_{\rm o} = \frac{iem_b}{2M_W s_{\rm w}}\Big\{[U_{\tilde{b}_{11}} U^*_{\tilde{b}_{22}}(\mu + \tan\beta A^*_b) - U_{\tilde{b}_{12}} U^*_{\tilde{b}_{21}}(\mu^* + \tan\beta A_b)]\Big(\delta Z_e - \frac{\delta M_W^2}{2M_W^2} - \frac{\delta s_{\rm w}}{s_{\rm w}}\Big)$$
$$+ i\,{\rm Im}\{U_{\tilde{b}_{11}} U^*_{\tilde{b}_{12}}(\mu + \tan\beta A^*_b)\}\delta Z^{\rm c}_{\tilde{b}_{12}} + i\,{\rm Im}\{U_{\tilde{b}_{21}} U^*_{\tilde{b}_{22}}(\mu + \tan\beta A^*_b)\}\delta Z^{\rm c*}_{\tilde{b}_{21}}$$
$$- \frac{1}{2}[U_{\tilde{b}_{11}} U^*_{\tilde{b}_{22}}(A^*_b - \mu\tan\beta) - U_{\tilde{b}_{12}} U^*_{\tilde{b}_{21}}(A_b - \mu^*\tan\beta)]\delta Z_{AG}\Big\}. \quad (81)$$

The renormalization condition reads [9,11]

$$\widetilde{\rm Re}\,\hat{\Lambda}(0, m^2_{\tilde{b}_1}, m^2_{\tilde{b}_1}) + \widetilde{\rm Re}\,\hat{\Lambda}(0, m^2_{\tilde{b}_2}, m^2_{\tilde{b}_2}) = 0, \quad (82)$$

which corresponds to the two conditions

$${\rm Re}\{\widetilde{\rm Re}\,\hat{\Lambda}(0, m^2_{\tilde{b}_1}, m^2_{\tilde{b}_1}) + \widetilde{\rm Re}\,\hat{\Lambda}(0, m^2_{\tilde{b}_2}, m^2_{\tilde{b}_2})\} = 0, \quad (83)$$

$${\rm Im}\{\widetilde{\rm Re}\,\hat{\Lambda}(0, m^2_{\tilde{b}_1}, m^2_{\tilde{b}_1}) + \widetilde{\rm Re}\,\hat{\Lambda}(0, m^2_{\tilde{b}_2}, m^2_{\tilde{b}_2})\} = 0. \quad (84)$$

The conditions (i)–(iv), are sufficient to fix all independent parameters and their respective counterterms. As in Sec. IV E, relating Eqs. (60) and (61), one derives Eqs. (62) and (63) which can also be written in the form

$${\rm Re}\{A^*_b - \mu\tan\beta\}\delta m_b = -m_b\,{\rm Re}\delta A_b - {\rm Re}\delta S + {\rm Im}U_+\,{\rm Im}\delta Y_b, \quad (85)$$

$${\rm Im}\{A^*_b - \mu\tan\beta\}\delta m_b = +m_b\,{\rm Im}\delta A_b - {\rm Im}\delta S + {\rm Re}U_-\,{\rm Im}\delta Y_b \quad (86)$$

with

$$\delta S = -m_b(\mu\,\delta\tan\beta + \delta\mu\tan\beta) - U^*_{\tilde{b}_{11}} U_{\tilde{b}_{12}}(\delta m^2_{\tilde{b}_1} - \delta m^2_{\tilde{b}_2}) - ({\rm Re}U_+ - i\,{\rm Im}U_-){\rm Re}\delta Y_b, \quad (87)$$

$$U_\pm = U_{\tilde{b}_{11}} U^*_{\tilde{b}_{22}} \pm U_{\tilde{b}_{12}} U^*_{\tilde{b}_{21}}. \quad (88)$$

$\delta m^2_{\tilde{b}_1}$ and $\delta m^2_{\tilde{b}_2}$ are fixed by Eqs. (42) and (40).

The above four Eqs. (83)–(86), can be solved for ${\rm Re}\delta A_b$, ${\rm Im}\delta A_b$, ${\rm Im}\delta Y_b$ and δm_b. Though, we still consider ${\rm Re}\delta A_b$ and ${\rm Im}\delta A_b$ as independent counterterms we first calculate ${\rm Im}\delta Y_b$ and δm_b in dependence of ${\rm Re}\delta A_b$ and ${\rm Im}\delta A_b$ for economically solving the systems of equations. The solution for ${\rm Im}\delta Y_b$ and δm_b is

$$\delta m_b = \frac{d_i f_r - d_r f_i}{e_r f_i - e_i f_r}, \quad (89)$$

$${\rm Im}\,\delta Y_b = \frac{d_r e_i - d_i e_r}{e_r f_i - e_i f_r}, \quad (90)$$

with

$$d_r = 2\tan\beta({\rm Im}U_+\,{\rm Im}\delta S - {\rm Re}U_-\,{\rm Re}\delta S) + 2\,{\rm Re}\Big[\frac{M_W s_{\rm w}}{ie}(2\delta Z_{\rm o} + \widetilde{\rm Re}\Lambda(0, m^2_{\tilde{b}_1}, m^2_{\tilde{b}_1}) + \widetilde{\rm Re}\Lambda(0, m^2_{\tilde{b}_2}, m^2_{\tilde{b}_2})) + \delta M + \delta Z_{\rm d} U_m\Big], \quad (91)$$

$$d_i = -2\tan\beta({\rm Re}U_+\,{\rm Im}\delta S + {\rm Im}U_-\,{\rm Re}\delta S + 2\,{\rm Im}\Big[\frac{M_W s_{\rm w}}{ie}(2\delta Z_{\rm o} + \widetilde{\rm Re}\Lambda(0, m^2_{\tilde{b}_1}, m^2_{\tilde{b}_1}) + \widetilde{\rm Re}\Lambda(0, m^2_{\tilde{b}_2}, m^2_{\tilde{b}_2})) + \delta M + \delta Z_{\rm d} U_m\Big], \quad (92)$$

$$e_r = +2\tan\beta[{\rm Im}U_+\,{\rm Im}\{A^*_b - \mu\tan\beta\} - {\rm Re}U_-\,{\rm Re}\{A^*_b - \mu\tan\beta\}] + 2\,{\rm Re}U_m, \quad (93)$$

$$e_i = -2\tan\beta[{\rm Re}U_+\,{\rm Im}\{A^*_b - \mu\tan\beta\} + {\rm Im}U_-\,{\rm Re}\{A^*_b - \mu\tan\beta\}] + 2\,{\rm Im}U_m, \quad (94)$$

$$f_r = -2\,{\rm Im}U_Y, \quad (95)$$

$$f_i = 2\tan\beta(|U_{\tilde{b}_{11}}|^2 - |U_{\tilde{b}_{12}}|^2) \quad (96)$$

and

$$U_m = U_{\tilde{b}_{11}} U^*_{\tilde{b}_{22}}(A^*_b\tan\beta + \mu) - U_{\tilde{b}_{12}} U^*_{\tilde{b}_{21}}(A_b\tan\beta + \mu^*). \quad (97)$$

From the Eqs. (85) and (86) we immediately obtain δA_b as

$${\rm Re}\delta A_b = \frac{1}{m_b}[+{\rm Im}\delta Y_b\,{\rm Im}U_+ - {\rm Re}\delta S - \delta m_b\,{\rm Re}\{A^*_b - \mu\tan\beta\}], \quad (98)$$

$${\rm Im}\delta A_b = \frac{1}{m_b}[-{\rm Im}\delta Y_b\,{\rm Re}U_- + {\rm Im}\delta S + \delta m_b\,{\rm Im}\{A^*_b - \mu\tan\beta\}]. \quad (99)$$

Finally, the $\bar{Z}$ factors in $\hat{\Lambda}$ have to be determined. The following condition is used

$$\widetilde{\rm Re}\hat{\Sigma}_{\tilde{b}_{ii}}(m^2_{\tilde{b}_1}) - \widetilde{\rm Re}\hat{\Sigma}_{\tilde{b}_{ii}}(m^2_{\tilde{b}_2}) = 0 \qquad (i = 1, 2). \quad (100)$$

This condition results in the following $\bar{Z}$ factors

$$\delta\bar{Z}_{\tilde{b}_{ii}} = -\frac{\widetilde{\mathrm{Re}}\Sigma_{\tilde{b}_{ii}}(m^2_{\tilde{b}_1}) - \widetilde{\mathrm{Re}}\Sigma_{\tilde{b}_{ii}}(m^2_{\tilde{b}_2})}{m^2_{\tilde{b}_1} - m^2_{\tilde{b}_2}} \quad (i=1,2), \quad (101)$$

which guarantees the IR finiteness of the renormalized vertex $\hat{\Lambda}$ [11].

Another subtlety has to be explained here: due to the fact that we have infrared divergent C functions at $p_1 = 0$ in $\Lambda(p_1^2 = 0, p^2, p^2)$, we must deal with vanishing gram determinants. Therefore we follow Ref. [40] (and references therein) and replace the corresponding C functions by well behaving linear combinations of B functions. Details can be found in the Appendix.

G. Parameter definition

The input parameters in the $b/\tilde{b}$ sector have to correspond to the chosen renormalization scheme. We start by defining the bottom-quark mass, where the experimental input is the SM $\overline{\mathrm{MS}}$ mass [41],

$$m_b^{\overline{\mathrm{MS}}}(m_b) = 4.2 \text{ GeV}. \quad (102)$$

The value of $m_b^{\overline{\mathrm{MS}}}(\mu_R)$ (at the renormalization scale μ_R) is calculated from $m_b^{\overline{\mathrm{MS}}}(m_b)$ at the three-loop level following the prescription given in Ref. [42].

An "on-shell" mass is derived from the $\overline{\mathrm{MS}}$ mass via

$$m_b^{\mathrm{OS}} = m_b^{\overline{\mathrm{MS}}}(\mu_R)\left[1 + \frac{\alpha_s^{\overline{\mathrm{MS}}}(\mu_R)}{\pi}\left(\frac{4}{3} + 2\ln\frac{\mu_R}{m_b^{\overline{\mathrm{MS}}}(\mu_R)}\right)\right]. \quad (103)$$

The $\overline{\mathrm{DR}}$ bottom-quark mass is calculated iteratively from[2]

$$m_b^{\overline{\mathrm{DR}}} = \frac{m_b^{\mathrm{OS}}(1+\Delta_b) + \delta m_b^{\mathrm{OS}} - \delta m_b^{\overline{\mathrm{DR}}}}{1+\Delta_b} \quad (104)$$

with an accuracy of $|1 - (m_b^{\overline{\mathrm{DR}}})^{(n)}/(m_b^{\overline{\mathrm{DR}}})^{(n-1)}| < 10^{-5}$ reached in the nth step of the iteration. The bottom-quark mass of a special renormalization scheme is then obtained from

$$m_b = m_b^{\overline{\mathrm{DR}}} + \delta m_b^{\overline{\mathrm{DR}}} - \delta m_b. \quad (105)$$

Here we have used

$$\begin{aligned}\delta m_b^{\mathrm{OS}} &= \tfrac{1}{2}\widetilde{\mathrm{Re}}\{m_b[\Sigma_b^L(m_b^2) + \Sigma_b^R(m_b^2)] \\ &\quad + [\Sigma_b^{SL}(m_b^2) + \Sigma_b^{SL}(m_b^2)]\}, \\ \delta m_b^{\overline{\mathrm{DR}}} &= \tfrac{1}{2}\widetilde{\mathrm{Re}}\{m_b[\Sigma_b^L(m_b^2) + \Sigma_b^R(m_b^2)]_{\mathrm{div}} \\ &\quad + [\Sigma_b^{SL}(m_b^2) + \Sigma_b^{SR}(m_b^2)]_{\mathrm{div}}\}, \end{aligned} \quad (106)$$

and δm_b as given in Secs. IV A, IV B, IV C, IV D, IV E, and IV F. The quantity Δ_b [44,45] resums the $\mathcal{O}((\alpha_s\tan\beta)^n)$ and $\mathcal{O}((\alpha_t\tan\beta)^n)$ terms and is given by

$$\begin{aligned}\Delta_b &= \frac{2\alpha_s(m_t)}{3\pi}\tan\beta M_3^* \mu^* I(m^2_{\tilde{b}_1}, m^2_{\tilde{b}_2}, m^2_{\tilde{g}}) \\ &\quad + \frac{\alpha_t(m_t)}{4\pi}\tan\beta A_t^* \mu^* I(m^2_{\tilde{t}_1}, m^2_{\tilde{t}_2}, |\mu|^2), \end{aligned} \quad (107)$$

with

$$I(a,b,c) = -\frac{ab\ln(b/a) + ac\ln(a/c) + bc\ln(c/b)}{(a-c)(c-b)(b-a)}. \quad (108)$$

Here α_t is defined in terms of the top Yukawa coupling $y_t(m_t) = \sqrt{2}m_t(m_t)/v$ as $\alpha_t(m_t) = y_t^2(m_t)/(4\pi)$ with $v = 1/\sqrt{\sqrt{2}G_F} = 246.218$ GeV and $m_t(m_t) \approx m_t/(1 - \frac{1}{2\pi}\alpha_t(m_t) + \frac{4}{3\pi}\alpha_s(m_t))$. M_3 is the soft SUSY-breaking parameter for the gluinos, with the gluino mass given as $m_{\tilde{g}} := |M_3|$.

V. RENORMALIZATION SCHEME ANALYSIS

A. Calculation of loop diagrams

In this section we give the relevant details about the calculation of the higher-order corrections to the decay channels (1) and (2). Sample diagrams are shown in Figs. 2 and 3. Not shown are the diagrams for real (hard or soft) photon and gluon radiation (which, however, can become numerically very important). They are obtained from the corresponding tree-level diagrams by attaching a photon (gluon) to the electrically (color) charged particles. The internal, in a generical way depicted particles in Figs. 2 and 3 are labeled as follows: F can be a SM fermion, a chargino or neutralino or a gluino, S can be a sfermion or a Higgs boson, V can be a photon γ, a Z or $W^\pm$ boson or a gluon g. Not shown are the diagrams with a gauge boson (Goldstone $G^\pm$)–Higgs self-energy contribution on the external Higgs boson leg that can appear in the decay $\tilde{t}_2 \to \tilde{b}_i H^+$. On the other hand, in our calculation, the wave function corrections for $\tilde{t}_2 \to \tilde{b}_i W^+$ vanish as all the external particle fields are renormalized on-shell.

The diagrams and corresponding amplitudes have been obtained with the program FEYNARTS [46]. The further evaluation has been performed with FORMCALC [47]. As regularization scheme for the UV divergences we have used constrained differential renormalization [48], which has been shown to be equivalent to dimensional reduction [49] at the one-loop level [47]. Thus the employed regularization preserves SUSY [50,51]. It was checked that all UV divergences cancel in the final result.

The IR divergences from diagrams with an internal photon or gluon have to cancel with the ones from the corresponding real soft radiation. In the case of QED we have included the soft photon contribution following the description given in Ref. [28]. In the case of QCD we have modified this prescription by replacing the product of electric charges by the appropriate combination of color charges (linear combination of C_A and C_F times α_s).

[2] In case of complex Δ_b the replacement $(1+\Delta_b) \to |1+\Delta_b|$ should be performed [43].

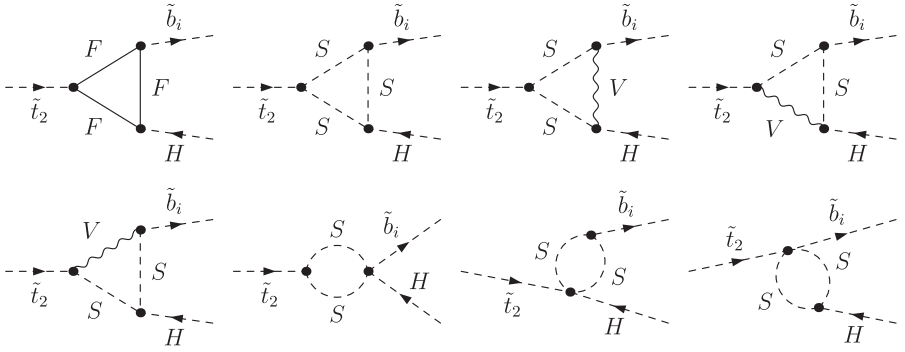

FIG. 2. Generic Feynman diagrams for the decay $\tilde{t}_2 \to \tilde{b}_i H^+$ ($i = 1, 2$). F can be a SM fermion, a chargino or neutralino or a gluino, S can be a sfermion or a Higgs boson, V can be a γ, Z, $W^\pm$ or g. Not shown are the diagrams with a $W^+ - H^+$ or $G^+ - H^+$ transition contribution on the external Higgs boson leg.

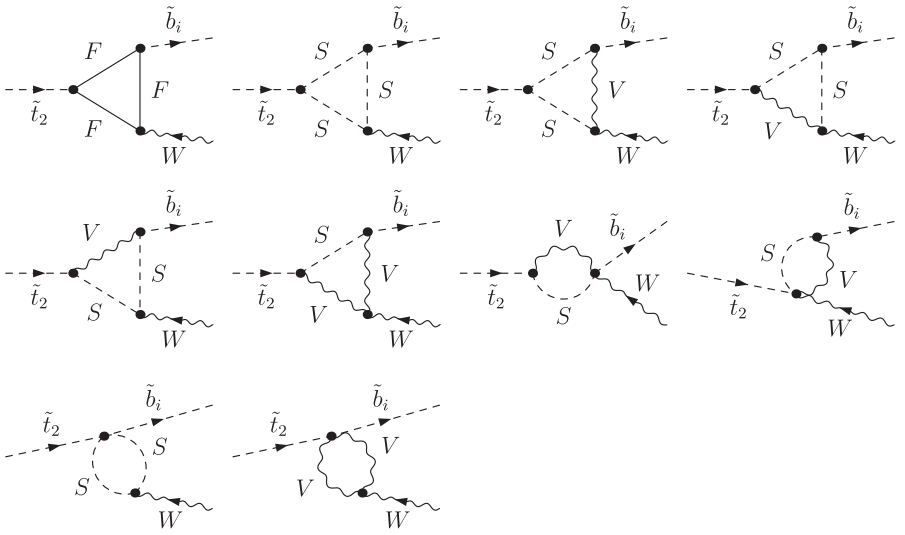

FIG. 3. Generic Feynman diagrams for the decay $\tilde{t}_2 \to \tilde{b}_i W^+$ ($i = 1, 2$). F can be a SM fermion, a chargino or neutralino or a gluino, S can be a sfermion or a Higgs boson, V can be a γ, Z, $W^\pm$ or g.

More details will be given in Ref. [26]. Using the sbottom masses at the one-loop level, see Sec. IV, we found cancellation beyond one-loop order of the related IR and UV divergences for the decay $\tilde{t}_2 \to \tilde{b}_i H^+$, and a cancellation, as required, at the one-loop level for the decay $\tilde{t}_2 \to \tilde{b}_i W^+$.[3]

For completeness we show here also the formulas that have been used to calculate the tree-level decay widths:

$$\Gamma^{\text{tree}}(\tilde{t}_2 \to \tilde{b}_i H^+) = \frac{|C(\tilde{t}_2, \tilde{b}_i, H^+)|^2 \lambda^{1/2}(m^2_{\tilde{t}_2}, m^2_{\tilde{b}_i}, M^2_{H^\pm})}{16\pi m^3_{\tilde{t}_2}} \quad (i = 1, 2), \tag{109}$$

$$\Gamma^{\text{tree}}(\tilde{t}_2 \to \tilde{b}_i W^+) = \frac{|C(\tilde{t}_2, \tilde{b}_i, W)|^2 \lambda^{3/2}(m^2_{\tilde{t}_2}, m^2_{\tilde{b}_i}, M^2_W)}{16\pi M^2_W m^3_{\tilde{t}_2}} \quad (i = 1, 2), \tag{110}$$

where $\lambda(x, y, z) = (x - y - z)^2 - 4yz$ and the couplings $C(a, b, c)$ can be found in the FEYNARTS model files [52]. The bottom-Yukawa couplings generically are enhanced with $\tan\beta$.

B. Numerical examples for the six renormalization schemes

We start our analysis by showing some representative numerical examples. We evaluate the tree-level results and the one-loop correction for $\Gamma(\tilde{t}_2 \to \tilde{b}_1 H^+)$ including

[3]Using tree-level masses yields a cancellation of IR divergences beyond one-loop order also for $\tilde{t}_2 \to \tilde{b}_i W^+$.

wave function corrections. The parameters are chosen according to the two scenarios, S1 and S2, shown in Table II.[4]

So far we concentrate on the rMSSM: if a scheme shows deficiencies in the rMSSM, the same problems occur in the cMSSM. The final numerical examples in Sec. VI will also show complex parameters as well as results for $\Gamma(\tilde{t}_2 \to \tilde{b}_{1,2} W^+)$. It should be noted that $\tan\beta \lesssim 9.6(4.6)$ is excluded for S1 (S2) due to the MSSM Higgs boson searches at LEP [54,55]. However, we are interested in the general behavior of the renormalization schemes. If certain features appear in the two numerical scenarios (S1 and S2) only for experimentally excluded $\tan\beta$ values, other parameter choices may exhibit these features also in unexcluded parts of the MSSM parameter space. Consequently, in order to investigate the various renormalization schemes on general grounds, in the following we show the results for $\tan\beta > 1$. A similar reasoning applies to the limits on the MSSM parameter space due to SUSY searches. Nevertheless, to avoid completely unrealistic spectra, the following exclusion limits [41] hold in our two scenarios:

$$m_{\tilde{t}_1} > 95 \text{ GeV}, \quad m_{\tilde{b}_1} > 89 \text{ GeV}, \quad m_{\tilde{q}} > 379 \text{ GeV},$$
$$m_{\tilde{e}_1} > 73 \text{ GeV}, \quad m_{\tilde{\chi}_1^0} > 46 \text{ GeV}, \quad m_{\tilde{\chi}_1^\pm} > 94 \text{ GeV},$$
$$m_{\tilde{g}} > 308 \text{ GeV}. \tag{111}$$

A few examples of the scalar top- and bottom-quark masses at the one-loop level[5] (using $M^2_{\tilde{Q}_L}(\tilde{b})$ in Eq. (44) for the one-loop result) in the scenarios S1 and S2 are shown in Table III. The values of $m_{\tilde{t}_2}$ allow copious production of the heavier scalar top-quark at the LHC. For other choices of the gluino mass, $m_{\tilde{g}} > m_{\tilde{t}_2}$, which would leave no visible effect for most of the decay modes of the $\tilde{t}_2$, the heavier scalar top-quark could also be produced from gluino decays at the LHC. Furthermore, in S1 (even for the nominal value of $m_{\tilde{t}_2}$ as given in Table II) the production of $\tilde{t}_2$ at the ILC (1000), i.e. with $\sqrt{s} = 1000$ GeV, via $e^+e^- \to \tilde{t}_2\tilde{t}_1$ will be possible, with the subsequent decay modes (1) and (2) being open. The clean environment of the ILC would permit a detailed study of the scalar top-quark decays. Depending on the combination of allowed decay channels a determination of the branching ratios at the few percent level might be achievable in the high-luminosity running of the ILC (1000). More details will be discussed elsewhere [26].

Later we will also analyze numerical results for complex input parameters. Here it should be noted that the results for physical observables are affected only by certain combinations of the complex phases of the parameters μ, the trilinear couplings A_f, $f = \{u, c, t, d, s, b, e, \mu, \tau\}$, the gaugino mass parameters M_1, M_2, M_3 and the Higgs soft SUSY-breaking parameter m_{12}^2 [56,57]. It is possible, for instance, to eliminate the phase φ_{M_2} and the phase $\varphi_{m_{12}^2}$. Experimental constraints on the (combinations of) complex phases arise, in particular, from their contributions to electric dipole moments of heavy quarks [58], of the electron and the neutron (see Refs. [59,60] and references therein), and of the deuteron [61]. While SM contributions enter only at the three-loop level, due to its complex phases the MSSM can contribute already at one-loop order. Large phases in the first two generations of sfermions can only be accommodated if these generations are assumed to be very heavy [62] or large cancellations occur [63], see however the discussion in Refs. [64,65]. A recent review can be found in Ref. [66]. Accordingly, using the convention that $\varphi_{M_2} = 0$ and $\varphi_{m_{12}^2} = 0$, as done in this paper, in particular, the phase φ_μ is tightly constrained [65], while the bounds on the phases of the third generation trilinear couplings are

TABLE II. MSSM parameters for the initial numerical investigation; all parameters are in GeV. We always set $m_b^{\overline{\rm MS}}(m_b) = 4.2$ GeV. In our analysis we use $M_{\tilde{Q}_L}(\tilde{t}) = M_{\tilde{t}_R} = M_{\tilde{b}_R} =: M_{\rm SUSY}$, where $M_{\rm SUSY}$ is chosen such that the above value of $m_{\tilde{t}_2}$ is realized. For the $\tilde{b}$ sector the shift in $M_{\tilde{Q}_L}(\tilde{b})$ as defined in Eq. (44) is taken into account. The parameters entering the scalar lepton sector and/or the first two generations do not play a relevant role in our analysis. The values for A_t and A_b are chosen such that charge- or color-breaking minima are avoided [53].

Scen.	$M_{H^\pm}$	$m_{\tilde{t}_2}$	μ	A_t	A_b	M_1	M_2	M_3
S1	150	600	200	900	400	200	300	800
S2	180	900	300	1800	1600	150	200	400

TABLE III. The top and bottom squark masses at the one-loop level (see text) in the scenarios S1 and S2 and at different $\tan\beta$ for the numerical investigation; all masses are in GeV and rounded to 1 MeV.

Scen.	$\tan\beta$	$m_{\tilde{t}_1}$	$m_{\tilde{t}_2}$	$m_{\tilde{b}_1}$	$m_{\tilde{b}_2}$
	2	293.391	600.000	441.987	447.168
S1	20	235.073	600.000	418.824	439.226
	50	230.662	600.000	400.815	449.638
	2	495.014	900.000	702.522	707.598
S2	20	445.885	900.000	678.531	695.180
	50	442.416	900.000	628.615	697.202

[4]It should be noted that we do not include any further shifts in the parameters than the one given in Eq. (44). Correspondingly, the values for the parameters A_b and $M_{\tilde{b}_R}$ in Table II do not reflect the actual values for the input parameters with respect to the chosen renormalization scheme. For example, the $\tilde{b}_2$ mass—though considered as an input in the renormalization scheme and defined as on-shell mass—receives a shift going from tree- to one-loop level when starting out with the values in Table II and including only the shift Eq. (44). To circumvent this shift of the $\tilde{b}_2$ mass, additional shifts to the tree-level values of A_b and $M_{\tilde{b}_R}$ would be required (depending on the renormalization scheme).

[5]For the scalar top-quark masses the tree-level and the one-loop values are the same (according to our renormalization conditions).

TABLE IV. Examples for tree-level and full one-loop contributions (see text) to $\Gamma(\tilde{t}_2 \to \tilde{b}_1 H^+)$ for S1 (upper table) and S2 (lower table); all values are in GeV (no comparison of the renormalization schemes, see text). In S1 using RS5 a divergence is reached for $\tan\beta = |A_b|/|\mu| = 2$ and no value can be computed (see text below). The different renormalization schemes are listed in Table I.

$\Gamma(\tilde{t}_2 \to \tilde{b}_1 H^+)$ for S1			$\tan\beta = 2$			$\tan\beta = 50$		
	Renorm. scheme	μ_R	tree	loop	m_b	tree	loop	m_b
RS1:	"OS"	$m_{\tilde{t}_2}$	0.0017	−0.0011	3.29	2.5930	−53.3469	3.84
RS2:	"m_b, $A_b\overline{\text{DR}}$"	$m_{\tilde{t}_2}$	0.0009	0.0002	2.38	0.9653	−0.0311	2.16
RS3:	"m_b, $Y_b\overline{\text{DR}}$"	$m_{\tilde{t}_2}$	0.0009	0.0004	2.38	0.9484	−1.5404	2.16
RS4:	"$m_b\overline{\text{DR}}$, Y_b OS"	$m_{\tilde{t}_2}$	0.0009	0.0000	2.38	0.9593	−0.3411	2.16
RS5:	"$A_b\overline{\text{DR}}$, ReY_b OS"	$m_{\tilde{t}_2}$	-	-	-	0.9399	−0.0481	2.13
RS6:	"A_b vertex, ReY_b OS"	$m_{\tilde{t}_2}$	0.0007	0.0001	2.19	0.9390	−0.0347	2.13

$\Gamma(\tilde{t}_2 \to \tilde{b}_1 H^+)$ for S2			$\tan\beta = 2$			$\tan\beta = 50$		
	Renorm. scheme	μ_R	tree	loop	m_b	tree	loop	m_b
RS1:	"OS"	$m_{\tilde{t}_2}$	2.0928	−0.0776	3.23	8.5163	−106.9700	3.70
RS2:	"m_b, $A_b\overline{\text{DR}}$"	$m_{\tilde{t}_2}$	2.2171	−0.1449	2.33	1.8173	−0.5125	2.11
RS3:	"m_b, $Y_b\overline{\text{DR}}$"	$m_{\tilde{t}_2}$	0.0077	0.0582	2.33	3.1409	−11.6833	2.11
RS4:	"$m_b\overline{\text{DR}}$, Y_b OS"	$m_{\tilde{t}_2}$	2.2564	−0.1031	2.33	2.9230	−4.5506	2.11
RS5:	"$A_b\overline{\text{DR}}$, ReY_b OS"	$m_{\tilde{t}_2}$	2.2332	−0.1004	2.45	2.3018	0.2924	1.84
RS6:	"A_b vertex, ReY_b OS"	$m_{\tilde{t}_2}$	2.2925	−0.1067	2.14	2.3558	−0.0710	1.86

much weaker. The phase of μ enters in the combinations $(\varphi_{A_{t,b}} + \varphi_\mu - \varphi_{m_{12}^2})$. Setting $\varphi_\mu = 0$ (and $\varphi_{M_2} = \varphi_{m_{12}^2} = 0$, see above) leaves us with A_t and A_b as complex valued parameters. Since we are interested in the renormalization of the $b/\tilde{b}$ sector, in our numerical analysis we will focus on a complex A_b and keep A_t real (see, however, Ref. [26]).

We start our numerical examples with the evaluation of $\Gamma(\tilde{t}_2 \to \tilde{b}_1 H^+)$ in S1 and S2 for $\tan\beta = 2$ and $\tan\beta = 50$ as shown in Table IV. The corresponding results as a continuous function of $\tan\beta$ can be seen in Fig. 4. It must be emphasized here that the table and the plots do not constitute a *comparison* of the various schemes, but "only" individual numerical examples that are used to exhibit certain problems of the various schemes. A numerical comparison of the schemes requires that the input parameters are converted from one scheme into another, see, for instance, Ref. [10], which is not performed within this analysis. In our numerical examples the renormalization scale, μ_R, has been set to the mass of the decaying particle, i.e. $\mu_R = m_{\tilde{t}_2}$. In Table IV the two main columns, labeled "$\tan\beta = 2$" and "$\tan\beta = 50$," are divided into three columns where "tree" contains the tree-level results and "loop" the one-loop contribution. m_b denotes the corrected bottom-quark value corresponding to the respective renormalization, see Eq. (105).

The two values of $\tan\beta$ were chosen as an example of a very low and a very high value. It should be kept in mind that the low value is possibly already in conflict with MSSM Higgs boson searches [54,55], but kept to show an "extreme" example as explained above. It can be seen

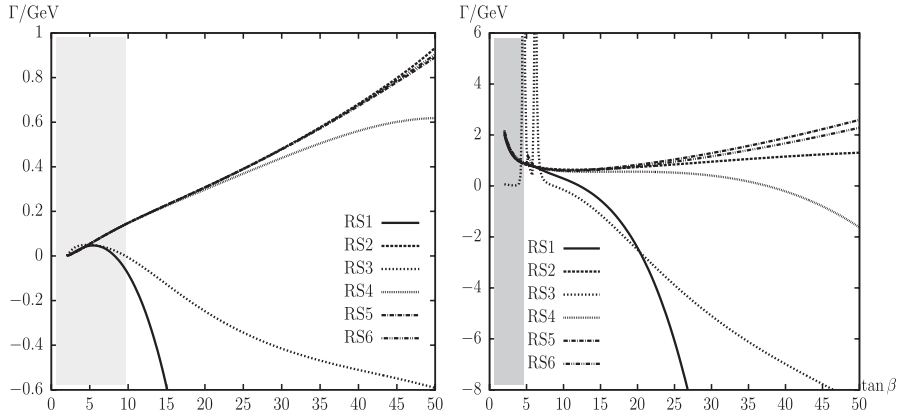

FIG. 4. $\Gamma(\tilde{t}_2 \to \tilde{b}_1 H^+)$. Full one-loop corrected partial decay widths for the different renormalization schemes (no comparison, see text). The parameters are chosen according to S1 in the left plot and S2 in the right plot. For S1 the grey region and for S2 the dark grey region is excluded by LEP Higgs searches (see text).

that RS1, RS3, RS4 and RS5 yield relatively large absolute values of loop contributions with respect to the tree-level result, either for $\tan\beta = 2$ *or* for $\tan\beta = 50$, at least in one of the two numerical scenarios. This simple example shows that (by choosing a specific scenario) already all except two renormalization schemes fail in part of the parameter space.

More problems of the renormalization schemes RS1, RS3, RS4, and RS5 become visible in Fig. 4. In the left (right) plot of Fig. 4 we show the results of S1(S2) as a function of $\tan\beta$. For S1 the grey region and for S2 the dark grey region at low values of $\tan\beta$ are excluded by LEP Higgs searches [55]. It can be seen in Fig. 4 that RS1 and RS3 deviate strongly from the (see the end of Sec. V A) expected behavior of increasing $\Gamma(\tilde{t}_2 \to \tilde{b}_1 H^+)$ with growing $\tan\beta$ that the other schemes exhibit. The same is observed for RS4 in S2 for $\tan\beta \gtrsim 35$. Problems in RS2 are discussed in Sec. V F, problems in RS6 have been found for complex parameters, see Sec. V G. The various spikes and dips can be understood as follows:

(i) For RS3 in S2 a "peak" appears at $\tan\beta \approx 4.6$ and at $\tan\beta \approx 6.2$. This is discussed in Sec. V E below.

(ii) For RS5 in S1 a peak appears (not visible) at $\tan\beta = |A_b|/|\mu| = 2$. This is caused by large corrections to the bottom-quark mass as discussed further in Sec. V G. This is also the reason why there is no entry in Table IV for RS5, S1 at $\tan\beta = 2$.

(iii) For RS5 in S2 a peak appears at $\tan\beta = |A_b|/|\mu| = 5.33$. This is caused by large corrections to the bottom-quark mass as discussed further in Sec. V G.

C. Generic considerations for the $b/\tilde{b}$ sector renormalization (I)

As discussed in Sec. IV, a bottom-quark/squark sector renormalization scheme always contains dependent counterterms which can be expressed by the independent ones. According to our six definitions, this can be δm_b, δA_b or δY_b. A problem can occur when the MSSM parameters are chosen such that the independent counterterms (nearly) drop out of the relation determining the dependent counterterms. As will be shown below, even restricting to the two numerical examples, S1 and S2, it is possible to find a set of MSSM parameters which show this behavior for each of the chosen renormalization schemes. Consequently, it appears to be difficult *by construction* to define a renormalization scheme for the bottom-quark/squark sector (once the top-quark/squark sector has been defined) that behaves well for the full MSSM parameter space. One possible exception could be a pure $\overline{\text{DR}}$ scheme, which, however, is not well suited for processes with external top squarks and/or bottom squarks.

Assuming that SUSY, and more specifically the MSSM, will be discovered at the LHC and its parameters will be measured, the problem will have disappeared. For a specific set of MSSM parameters, renormalization schemes can (easily) be found that behave well. However, due to our ignorance about the actual values of the SUSY parameters, scans over large parts of the MSSM parameter space are performed, see also Sec. VI. For this kind of analysis a careful choice of the renormalization scheme has to be made.

In the following subsections we will analyze in more detail, analytically and numerically, the deficiencies of the various schemes.

D. Problems of the "OS" renormalization

The "OS" renormalization as described in Sec. IV A does not yield reasonable results in perturbative calculations as shown already, e.g. in Refs. [10,11]. For the sake of completeness we briefly repeat the results. The "OS" scheme of Sec. IV A is the renormalization scheme analogous to the one used in the $t/\tilde{t}$ sector and thus would be the "naive" choice. It includes an on-shell renormalization condition on the sbottom mixing parameter Y_b that contains the combination $(A_b - \mu^* \tan\beta)$. In parameter regions where $(\mu \tan\beta))$ is much larger than A_b, the counterterm δA_b receives a very large finite shift when calculated from the counterterm δY_b. More specifically, δA_b as given in Eq. (48) contains the contribution

$$\delta A_b = \frac{1}{m_b}[-(A_b - \mu^* \tan\beta)\delta m_b + \ldots] \tag{112}$$

that can give rise to very large corrections to A_b. This is also visible in Fig. 5 below, where we show the numerical values of δA_b as a function of $\tan\beta$ for various renormalization schemes. In Ref. [10] it was shown that, because of Eq. (112), the "OS" renormalization yields huge corrections to the lightest MSSM Higgs mass. Also the numerical results shown in Table IV and Fig. 4 show extremely large one-loop corrections for $\tan\beta = 50$.

This problem is (more or less) avoided in the other renormalization schemes introduced in Table I, where the renormalization condition is applied directly to A_b, rather than deriving δA_b from a renormalization condition fixing δY_b. Also the renormalization schemes RS3 ("m_b, $Y_b\overline{\text{DR}}$") and RS4 ("$m_b\overline{\text{DR}}$, Y_b OS") avoid this severe problem by renormalizing the bottom-quark mass $\overline{\text{DR}}$.

E. Problems of non-A_b renormalization schemes

Two of our schemes, besides the "OS" scheme (RS1), do not employ a renormalization of A_b: RS3 ("m_b, $Y_b\overline{\text{DR}}$") and RS4 ("$m_b\overline{\text{DR}}$, Y_b OS"). As argued in Sec. V D a huge contribution to δA_b as evaluated in that section is avoided by the $\overline{\text{DR}}$ renormalization of m_b. However, following Eq. (48) with $\delta m^2_{\tilde{b}_1}$, $\delta m^2_{\tilde{b}_2}$, δY_b and δm_b chosen according to the renormalization schemes RS3 and RS4, respectively, one finds for the finite parts of δA_b:

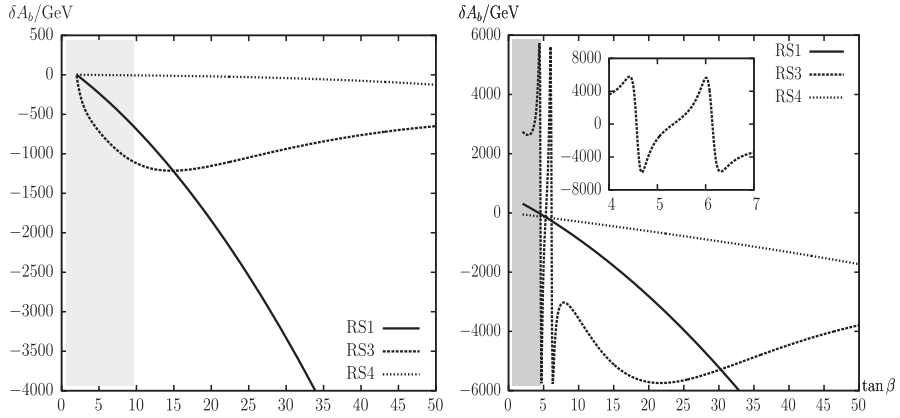

FIG. 5. Finite parts of δA_b in various renormalization schemes. The parameters are chosen according to S1 left plot and S2 right plot. For S1 the grey region is excluded and for S2 the dark grey region is excluded.

$$\text{RS 3: } \delta A_b|_{\text{fin}} = \frac{1}{m_b}[U_{\tilde{b}_{11}} U^*_{\tilde{b}_{12}} (\delta m^2_{\tilde{b}_1} - \delta m^2_{\tilde{b}_2})]_{\text{fin}} + \ldots, \tag{113}$$

$$\text{RS 4: } \delta A_b|_{\text{fin}} = \frac{1}{m_b}[U_{\tilde{b}_{11}} U^*_{\tilde{b}_{12}} (\delta m^2_{\tilde{b}_1} - \delta m^2_{\tilde{b}_2}) + U_{\tilde{b}_{11}} U^*_{\tilde{b}_{22}} \delta Y^*_b + U^*_{\tilde{b}_{12}} U_{\tilde{b}_{21}} \delta Y_b]_{\text{fin}} + \ldots, \tag{114}$$

where the ellipses denote contributions from $\delta\mu$ which, however, are not relevant for our argument. It can be seen that still δA_b depends on parameters (diagonal and off-diagonal sbottom self-energies) that are independent of A_b. As an example, Higgs boson loops in the sbottom self-energy contain contributions $\sim\mu\tan\beta$, which can become very large, independently of the value of A_b. This can be seen in the right plot of Fig. 5, where we show δA_b as a function of $\tan\beta$ in S2. In both renormalization schemes, RS3 and RS4, δA_b becomes very large and negative for large $\tan\beta$. This yields the very large and negative loop corrections to $\Gamma(\tilde{t}_2 \to \tilde{b}_1 H^+)$ shown in the right plot of Fig. 4. In S1 this problem is less pronounced, as can be seen in the left plot of Fig. 5 (δA_b) and Fig. 4 ($\Gamma(\tilde{t}_2 \to \tilde{b}_1 H^+)$).

But also for lower $\tan\beta$ values, $\tan\beta \lesssim 10$, problems can occur. The (finite) ''multiple spike structure'' in RS3 for S2 around $\tan\beta \approx 5.33$ (for details see the small insert within the right plot of Fig. 5) is due to an interplay of top/chargino contributions to the two diagonal sbottom self-energies, invalidating this scenario also for this part of the parameter space.

F. Problems of an $m_b - A_b$ renormalization

If m_b and A_b are renormalized, the sbottom mixing parameter Y_b is necessarily a dependent parameter, see Table I. This situation is realized in the scheme RS2 (''m_b, $A_b\overline{\text{DR}}$''), see Sec. IV B. δY_b enters prominently into $\delta Z_{\tilde{b}_{21}}$. For real parameters we have,

$$\delta Z_{\tilde{b}_{21}} = -2\frac{\text{Re}\Sigma_{\tilde{b}_{21}}(m^2_{\tilde{b}_2}) - \delta Y_b}{m^2_{\tilde{b}_1} - m^2_{\tilde{b}_2}}. \tag{115}$$

In this way δY_b (or the interplay between δY_b and $\text{Re}\Sigma_{\tilde{b}_{21}}(m^2_{\tilde{b}_2})$) can induce large loop corrections to the scalar top-quark decay width. δY_b can be decomposed according to Eq. (51) (concentrating again on the case of real parameters),

$$\delta Y_b = \frac{U_{\tilde{b}_{11}} U_{\tilde{b}_{21}}}{|U_{\tilde{b}_{11}}|^2 - |U_{\tilde{b}_{12}}|^2}(\delta m^2_{\tilde{b}_1} - \delta m^2_{\tilde{b}_2}) + \ldots, \tag{116}$$

where the ellipses denote terms with only divergent contributions (due to the chosen renormalization scheme RS2) as well as finite contributions from $\delta\mu$, which, however, do not play a role for our argument. For ''maximal sbottom mixing'', $|U_{\tilde{b}_{11}}| \approx |U_{\tilde{b}_{12}}|$, δY_b diverges, and the loop calculation does not yield a reliable result. In our two parameter scenarios, S1 and S2, this is not the case. Such a large sbottom mixing is often associated with large values of $|A_b|$ that may be in conflict with charge- or color-breaking minima [53].

However, in order to show an example with a divergence in δY_b we use a modified version of S1 with $A_b = 1000$ GeV (a value still allowed following Ref. [53]). In this scenario at $\tan\beta \approx 37$ we indeed find the case of ''maximal mixing'' in the scalar bottom sector. As expected this leads to a divergence in δY_b, as can be seen in the left plot of Fig. 6. This divergence propagates into $\delta Z_{\tilde{b}_{21}}$ as shown in the right plot of Fig. 6.[6] (Also $\Sigma_{\tilde{b}_{21}}$ exhibits a discontinuity due to a sign change in $U_{\tilde{b}}$ for this extreme set of MSSM parameters.) The $\tan\beta$ value for which this ''divergence'' occurs depends on the choice of the other MSSM parameters. For (numerical) comparison we also show $\delta Z_{\tilde{t}_{21}}$ for the two scenarios.

[6]The scalar bottom masses could receive large corrections via $M^2_{\tilde{Q}_L}(\tilde{b})$ in Eq. (44), with δY_b entering via Eq. (45).

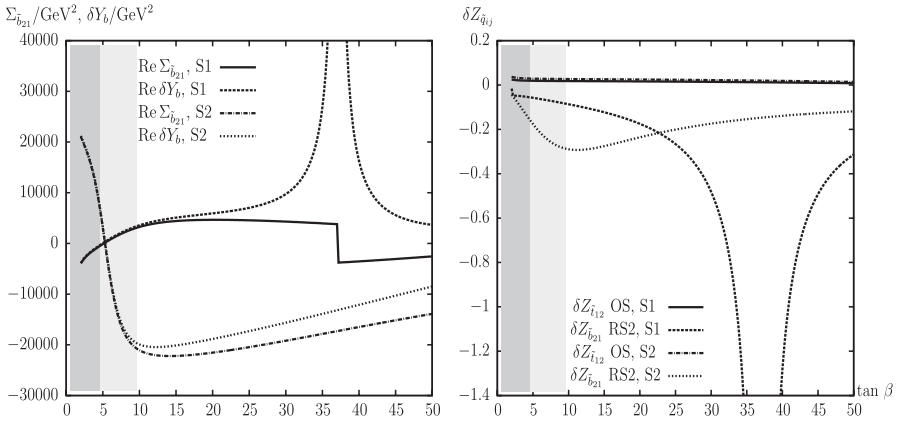

FIG. 6. $\Gamma(\tilde{t}_2 \to \tilde{b}_1 H^+)$. Left plot: size of δY_b and $\mathrm{Re}\Sigma_{\tilde{b}_{21}}(m^2_{\tilde{b}_1})$, the two contributions to $\delta Z_{\tilde{b}_{21}}$, in RS2. Right plot: comparison of the size of $\delta Z_{\tilde{b}_{21}}$ in the scheme RS2 ("m_b, $A_b\overline{\mathrm{DR}}$"). For both plots the parameters are chosen according to S1 (but here with $A_b = 1000$ GeV), S2 in Table II. For S1 the grey region is excluded and for S2 the dark grey region is excluded via LEP Higgs searches (see text).

For the different choice of MSSM parameters in S2 (without a higher A_b value) this divergences does not occur. However, for $\tan\beta \lesssim 7$ one finds $\delta Y_b \gtrsim \mathrm{Re}\Sigma_{\tilde{b}_{21}}(m^2_{\tilde{b}_1})$ (with $\delta Y_b = \mathrm{Re}\Sigma_{\tilde{b}_{21}}(m^2_{\tilde{b}_1})$ for $\tan\beta \approx 7.5$). In this part of the parameter space we also find $m_{\tilde{b}_1} \approx m_{\tilde{b}_2}$, yielding a relatively large value of $\delta Z_{\tilde{b}_{21}}$ according to Eq. (115), as can be seen in the right plot of Fig. 6. This relatively large (negative) value of $\delta Z_{\tilde{b}_{21}}$ in turn induces relatively large corrections to $\Gamma(\tilde{t}_2 \to \tilde{b}_1 H^+)$. However, the loop corrections do not exceed the tree-level value of $\Gamma(\tilde{t}_2 \to \tilde{b}_1 H^+)$ (for our choice of MSSM parameters). In summary: while for S1 a divergence in δY_b and thus in $\delta Z_{\tilde{b}_{12}}$ can appear for very large values of $|A_b|$ (possibly in conflict with charge- or color-breaking minima), invalidating the renormalization scheme RS2 in this part of the parameter space, these kind of problems are not encountered in S2. Here only moderate loop corrections to the respective tree-level values are found, and RS2 can be applied safely.

G. Problems of non-m_b renormalization schemes

Two of our schemes do not employ a renormalization condition for m_b: RS5 ("$A_b\overline{\mathrm{DR}}$, $\mathrm{Re}Y_b$ OS") and RS6 ("A_b vertex, $\mathrm{Re}Y_b$ OS"). Since A_b and Y_b are complex, we chose to renormalize A_b and the real part of Y_b.

We start with the discussion of the (simpler) "$A_b\overline{\mathrm{DR}}$, $\mathrm{Re}Y_b$ OS" scheme. We will focus on the real case as a subclass of the more general complex case. In this renormalization scheme the bottom-quark mass counterterm has the following form for real parameters (compare to Eq. (65)),

$$\delta m_b = -\frac{m_b \delta A_b + \delta S}{(A_b - \mu \tan\beta)}. \tag{117}$$

For vanishing sbottom mixing one finds $(A_b - \mu\tan\beta) \to 0$. In the "$A_b\overline{\mathrm{DR}}$, $\mathrm{Re}Y_b$ OS" scheme this yields a finite (and negative) numerator in Eq. (117), but a vanishing denominator.

In a numerical evaluation, starting out with a value for the bottom-quark mass defined as $\overline{\mathrm{DR}}$ parameter, the actual value of the bottom-quark mass receives a shift with respect to the $\overline{\mathrm{DR}}$ bottom-quark mass according to Eq. (105). This shift corresponds to the finite part of δm_b in Eq. (117). Consequently, large positive or negative contributions to the bottom-quark mass can occur, yielding possibly negative values for the bottom-quark mass and thus invalidating the renormalization scheme for these parts of the parameter space. This can be seen in the left plot of Fig. 7, where we show m_b in RS5 (and RS6) for the two numerical scenarios given in Table II as a function of $\tan\beta$. m_b exhibits a strong upward/downward shift around the pole reached for $\tan\beta = A_b/\mu$ and consequently yields unreliable results in this part of the parameter space.

We now turn to the RS6 ("A_b vertex, $\mathrm{Re}Y_b$ OS") scheme. Following the same analysis as for the "$A_b\overline{\mathrm{DR}}$, $\mathrm{Re}Y_b$ OS" scheme an additional term in the denominator of the bottom-quark mass counterterm $\sim U_m/U_-$ appears,

$$\delta m_b = -\frac{\delta S + F}{(A_b - \mu\tan\beta) - U_m/(\tan\beta U_-)}, \tag{118}$$

where F denotes other (relatively small) additional contributions. With the help of Eq. (97) one finds for real parameters

$$\frac{U_m}{\tan\beta U_-} = \frac{U_{\tilde{b}_{11}} U_{\tilde{b}_{22}} (A_b \tan\beta + \mu) - U_{\tilde{b}_{12}} U_{\tilde{b}_{21}} (A_b \tan\beta + \mu)}{\tan\beta (U_{\tilde{b}_{11}} U_{\tilde{b}_{22}} - U_{\tilde{b}_{12}} U_{\tilde{b}_{21}})} = (A_b + \mu/\tan\beta), \tag{119}$$

and therefore

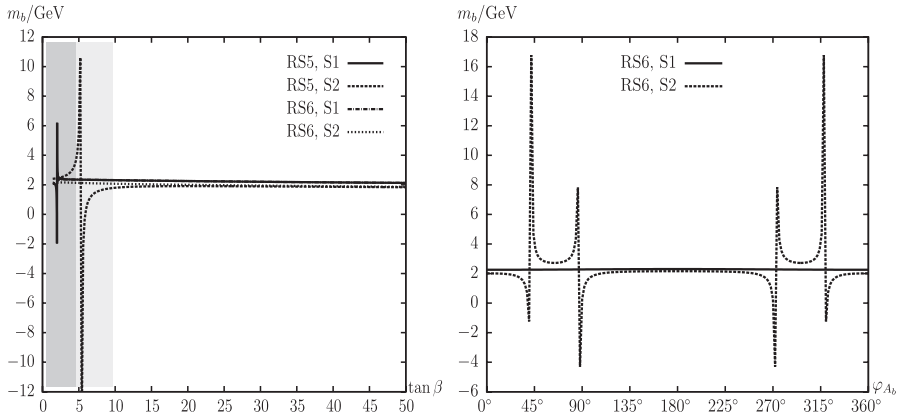

FIG. 7. Left plot: m_b in RS5 and RS6 for S1, S2. For S1 the grey region is excluded and for S2 the dark grey region is excluded. Right plot: m_b in RS6 for S1, S2 but both with $\tan\beta = 20$ and φ_{A_b} varied. In S2 we used also $|\mu| = 120$ GeV.

$$\delta m_b = \frac{\delta S + F}{\mu(\tan\beta + 1/\tan\beta)}. \tag{120}$$

The denominator of Eq. (120) can go to zero only for $\mu \to 0$, which is experimentally already excluded. Consequently, the problem of (too) large contributions to m_b is avoided in this scheme. This can be seen in the left plot of Fig. 7, where RS6, contrary to RS5, does not exhibit any polelike structure in m_b.

In the complex case the above argument is no longer valid, and larger contributions to δm_b can arise. In the limit of $\tan\beta \gg 1$ and μ real the denominator of δm_b in Eq. (89) reads

$$\frac{1}{\delta m_b} \sim 4\mu\tan^3\beta\Big[\mathrm{Re}U_-(|U_{\tilde{b}_{11}}|^2 - |U_{\tilde{b}_{12}}|^2) + \mathrm{Im}U_- \frac{4m_b}{m^2_{\tilde{b}_1} - m^2_{\tilde{b}_2}} \mathrm{Im}(U^*_{\tilde{b}_{11}} U_{\tilde{b}_{12}} A_b)\Big]. \tag{121}$$

Depending on φ_{A_b} this denominator can go to zero and thus yield unphysically large corrections to m_b in RS6. In the right plot of Fig. 7 we show m_b as function of φ_{A_b}. At $\varphi_{A_b} \approx 41.5°, 87.5°, 272.5°, 318.2°$ the denominator in Eq. (121) goes to zero and changes its sign which explains the corresponding structures. This divergence in δm_b enters via Eq. (105) already into the tree-level prediction. To summarize: while in S1 the scheme RS6 is well behaved and can be safely applied (also for complex A_b), in S2 (with $|\mu| = 120$ GeV) severe problems (divergences in the counterterms) arise once complex parameters are taken into account. Consequently, for S2 the scheme RS6 cannot be applied.

It should be noted that the "A_b vertex, ReY_b OS" (RS6) scheme is the complex version of the renormalization scheme used in Refs. [10,11] for the $\mathcal{O}(\alpha_b\alpha_s)$ corrections to the neutral Higgs boson self-energies and thus to the mass of the lightest MSSM Higgs boson, M_h. For real parameters, no problems occurred. Therefore, employing this renormalization scheme in Refs. [10,11] yields numerically stable results.

H. Generic considerations for the $b/\tilde{b}$ sector renormalization (II)

In the previous subsections we have analyzed analytically (and numerically) the deficiencies of the various renormalization schemes. We have shown that despite of the variety of schemes, even concentrating on the two sets of parameters, S1 and S2, severe problems can be encountered in all schemes.

For the further numerical evaluation of the partial stop quark decay widths we choose RS2 as our "preferred scheme." According to our analyses in the previous subsections, RS2 shows the "relatively most stable" behavior, problems only occur for maximal sbottom mixing, $|U_{\tilde{b}_{11}}| = |U_{\tilde{b}_{12}}|$, where a divergence in δY_b appears. Having δY_b as a dependent counterterm induces effects in the field renormalization constants $\delta Z_{\tilde{b}_{12}}$ and $\delta Z_{\tilde{b}_{21}}$ and in $\delta M^2_{\tilde{Q}_L}(\tilde{b})$ entering the scalar bottom-quark masses. In a process with only internal scalar bottom quarks, no problems occur due to the field renormalization, but counterterms to propagators, which induce a transition from a $\tilde{b}_1$ squark to a $\tilde{b}_2$ squark contain also the term δY_b. However, δY_b appearing in counterterms of *internal* scalar bottom quarks does not exhibit a problem, since in this case these "dangerous" contributions cancel (which we have checked analytically). On the other hand, other schemes with δm_b or δA_b as dependent counterterms may exhibit problems in larger parts of the parameter space and may induce large effects, since m_b (or the bottom-Yukawa coupling) and A_b enter prominently into the various couplings of the Higgs bosons to other particles.

We are not aware of any paper dealing with scalar quark decays (or decays into scalar quarks) that has employed exactly RS2 (or its real version), see our discussion in the beginning of Sec. IV. Very recently a calculation of the scalar top decay width in the rMSSM using a pure $\overline{\mathrm{DR}}$ scheme for all parameters was reported [67].

VI. NUMERICAL EXAMPLES FOR OUR FAVORITE SCHEME

Following the discussion in Sec. V we pick the renormalization scheme that shows the "most stable" behavior over the MSSM parameter space. We choose the "m_b, $A_b\overline{\rm DR}$"(RS2) scheme. Tree-level values of the partial decay widths shown in this section have been obtained including a shift in m_b according to Eq. (105). We will concentrate on the calculation of the partial $\tilde{t}_2$ decay widths including one scalar bottom quark in the final state. A calculation of the respective branching ratios requires the evaluation of *all* partial scalar top-quark decay widths, which in turn requires the renormalization of the full cMSSM. This is beyond the scope of our paper and will be presented elsewhere [26].

A. Full one-loop results

We start our numerical analysis with the upper left plot of Fig. 8, where we show the partial decay width $\Gamma(\tilde{t}_2 \to \tilde{b}_1 H^+)$ as a function of $\tan\beta$. "Tree" denotes the tree-level value and "full" is the decay width including *all* one-loop corrections as described in Sec. V A. As one can see, the full one-loop corrections are negative and rather small over the full range of $\tan\beta$, the largest size of the loop corrections is found to be $\sim$28% of the tree-level value for $\tan\beta = 50$ in S2.[7] In S1 the grey region and in S2 the dark grey region is excluded due to too small values of the mass of the lightest MSSM Higgs boson, M_h.

In the upper right plot of Fig. 8 we show the partial decay width varying $|A_b|$ for $\tan\beta = 20$. In S1 and S2 the full one-loop corrections grow with A_b, but never exceed $\sim$25% of the tree-level result. Note, that for S1 $|A_b| > 1130$ GeV (grey region) and S2 $|A_b| > 1800$ GeV (dark grey region) is excluded due to the charge- or color-breaking minima. Over the full parameter space the loop corrections are smooth and small with respect to the tree-level results.

In the lower left plot of Fig. 8 we analyze the partial decay width varying $|\mu|$ for $\tan\beta = 20$. Values for $|\mu| \lesssim 120$ GeV are excluded due to $m_{\tilde{\chi}_1^\pm} < 94$ GeV [41]. The loop corrected predictions for the partial decay width show several dips and spikes. In S1 the first dip at $|\mu| \approx 285$ GeV is due to $|U_{\tilde{b}_{11}}| \approx |U_{\tilde{b}_{12}}|$, see the discussion in Sec. V F. The second peak/dip (already present in the tree-level prediction) at $|\mu| = 300$ GeV is due to the renormalization of μ [12] and will be discussed in more detail in Ref. [26].[8] The third dip at $|\mu| \approx 424$ GeV, which is hardly visible, is due to the production threshold $m_t + m_{\tilde{\chi}_3^0} = m_{\tilde{t}_2}$. The fourth dip at $|\mu| \approx 873$ GeV is the threshold $m_{\tilde{t}_1} + M_{H^\pm} = m_{\tilde{b}_1}$ of the self-energy $\Sigma_{\tilde{b}_{11}}(m^2_{\tilde{b}_1})$ in the renormalization constants $\delta Z_{\tilde{b}_{11}}$ and $\delta m^2_{\tilde{b}_1}$. The fifth dip at $|\mu| \approx 1107$ GeV is the production threshold $m_{\tilde{b}_2} + M_W = m_{\tilde{t}_2}$. For $|\mu| > 790$ GeV the value of M_h drops strongly, and the scenario S1 is excluded by LEP Higgs searches as indicated by the gray shading. Apart from the dips analyzed above the loop corrections are very small and do not exceed $\sim$7% of the tree-level result, the prediction for $\Gamma(\tilde{t}_2 \to \tilde{b}_1 H^+)$ is well under control. We now turn to the scenario S2. Here, for growing $|\mu|$, the squark mass splitting in the $\tilde{t}/\tilde{b}$ sector becomes very large, leading to large contributions to the electroweak precision observables. The dark gray region for $|\mu| > 1060$ GeV yields W boson masses outside the experimentally favored region at the 2σ level, $M_W \gtrsim 80.445$ GeV [68]. Such large $|\mu|$ values are consequently disfavored. The dip/peak at $|\mu| = 200$ GeV in the tree and the loop contribution is due to $\delta\mu$, where $\mu = M_2$ is reached, see above. The second dip at $|\mu| = 477$ GeV, which is hardly visible, is the threshold $m_t + m_{\tilde{\chi}_2^\pm} = m_{\tilde{b}_1}$ of the self-energy $\Sigma_{\tilde{b}_{11}}(m^2_{\tilde{b}_1})$ in the renormalization constants $\delta Z_{\tilde{b}_{11}}$ and $\delta m^2_{\tilde{b}_1}$. The third dip at $|\mu| = 725$ GeV is the production threshold $m_t + m_{\tilde{\chi}_3^0} = m_{\tilde{t}_2}$. The fourth dip at $|\mu| = 850$ GeV is again the threshold $m_{\tilde{t}_1} + M_{H^\pm} = m_{\tilde{b}_1}$. In S2 the one-loop corrections are negative and growing with $|\mu|$. Apart from the dips described above, also in this numerical evaluation the loop corrections stay mostly relatively small with respect to the tree-level result, reaching the largest relative contribution at the smallest $|\mu|$ values, and are thus well under control.

We now turn to the case of complex parameters. As discussed in Sec. V B we consider only A_b as a complex parameter. In the lower right plot of Fig. 8 we show the partial decay width depending on φ_{A_b} for $\tan\beta = 20$. In S1, the tree-level values and the loop corrections are well-behaved. The latter ones stay relatively small for the whole parameter space, not exceeding $\sim$18% of the tree-level result. In S2, the largest corrections occur for real positive values of A_b and reach $\sim$12% of the tree-level values. For negative A_b, the tree-level result becomes very small (< 0.01 GeV) and here the size of the loop corrections can be as large as the tree-level values. A small (and barely visible) asymmetry in the one-loop corrections appears in the lower right plot of Fig. 8, due to terms $\sim U_{\tilde{b}_{ij}} \times C_{0,1,2}$ function. The peak/dip at $\varphi_{A_b} \approx 117°, 243°$ are again due to $|U_{\tilde{b}_{11}}| \approx |U_{\tilde{b}_{12}}|$, see Sec. V F. It can be seen that the peaks due to this divergence are relatively sharp, i.e. the region of parameter space that is invalidated remains relatively small.

In Fig. 9 we show the results for $\Gamma(\tilde{t}_2 \to \tilde{b}_2 H^+)$ for the same set and variation of parameters as above.

[7] It is interesting to note that at $\tan\beta = |A_b|/|\mu| = 2(5.33)$ in S1 (S2) we get $U_{\tilde{b}_{11,22}} = 1$ and $U_{\tilde{b}_{12,21}} = 0$, and consequently $\tilde{b}_{L,R} = \tilde{b}_{1,2}$, respectively.

[8] The chosen renormalization exhibits a divergence for $\mu = M_2$. $\delta\mu$ enters via δY_b into $\delta M^2_{\tilde{Q}_L}(\tilde{b})$ and thus into the values of $m_{\tilde{b}_i}$. Consequently, the dip is already present in the tree-level result.

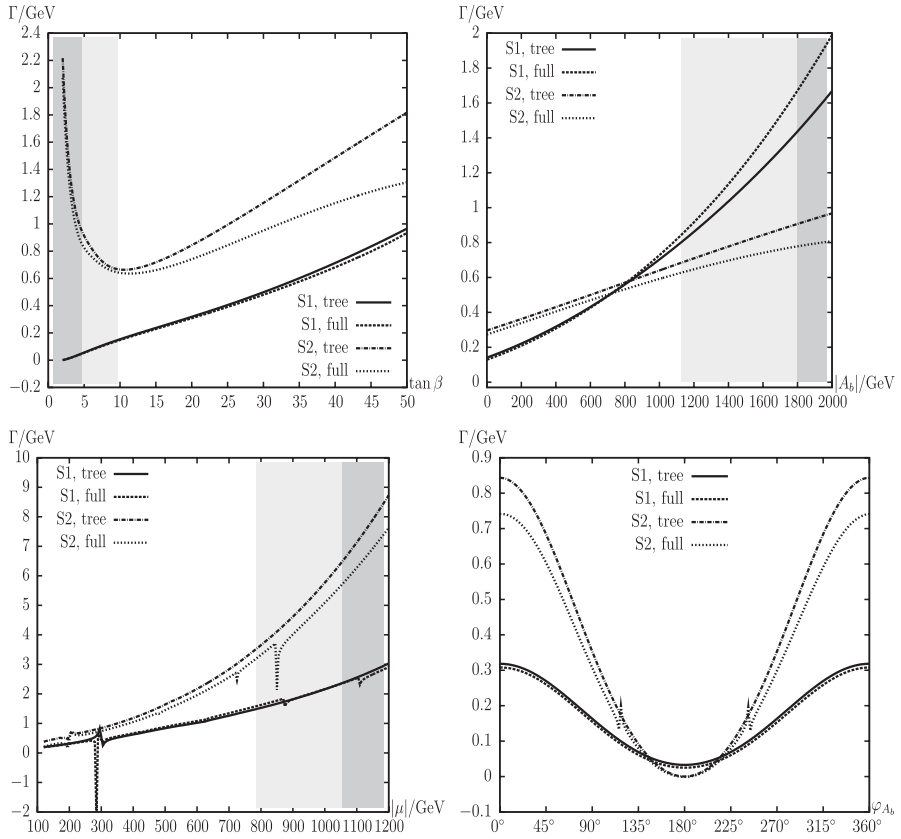

FIG. 8. $\Gamma(\tilde{t}_2 \to \tilde{b}_1 H^+)$. Tree-level and full one-loop corrected partial decay widths for the renormalization scheme RS2. The parameters are chosen according to the scenarios S1 and S2 (see Table II). For S1 the grey region is excluded and for S2 the dark grey region is excluded. Upper left plot: $\tan\beta$ varied. Upper right plot: $\tan\beta = 20$ and $|A_b|$ varied. Lower left plot: $\tan\beta = 20$ and $|\mu|$ varied. Lower right plot: $\tan\beta = 20$ and φ_{A_b} varied.

Consequently, the same peak and dip structures are visible in the lower plots of Fig. 9. In the lower left plot of Fig. 9 in S1 both lines end because the phase space closes, $m_{\tilde{b}_2} + M_{H^\pm} > m_{\tilde{t}_2}$ for $|\mu| > 300$ GeV. Overall the partial decay width is much smaller than for $\Gamma(\tilde{t}_2 \to \tilde{b}_1 H^+)$, which can partially be attributed to the smaller phase space, see for instance the results within S2 in the upper left plot of Fig. 9, and partially to the smallness of the tree-level coupling. Only in S2 for $\tan\beta \gtrsim 35$ we find $\Gamma(\tilde{t}_2 \to \tilde{b}_2 H^+) \gtrsim 1$ GeV. The relative corrections become very large for $|A_b| \gtrsim 1200$ GeV as shown in the upper right plot of Fig. 9, however these values are disfavored by the constraints from charge and color-breaking minima as discussed above. The smallness of $\Gamma(\tilde{t}_2 \to \tilde{b}_2 H^+)$ at the tree-level can lead sometimes to a ''negative value at the loop level''. In this case of (accidental) smallness of the tree-level partial decay width also $|\mathcal{M}_{\text{loop}}|^2$ would have to be taken into account, yielding a positive value for $\Gamma(\tilde{t}_2 \to \tilde{b}_2 H^+)$. Overall, because of the smallness of the tree-level result due to the tree-level coupling the *relative* size of the loop corrections are a bit larger than for $\Gamma(\tilde{t}_2 \to \tilde{b}_1 H^+)$. Nevertheless, apart from the peaks visible in the lower plots of Figs. 9, the loop corrections are well under control also for $\Gamma(\tilde{t}_2 \to \tilde{b}_2 H^+)$ using the renormalization scheme RS2. Again a small asymmetry in the one-loop corrections in the lower right plot of Fig. 9 can be observed, which is due to terms $\sim U_{\tilde{b}_{ij}} \times C_{0,1,2}$ function.

Finally we evaluate the partial decay width of a scalar top quark to a scalar bottom quark and a W boson, $\Gamma(\tilde{t}_2 \to \tilde{b}_1 W^+)$ and $\Gamma(\tilde{t}_2 \to \tilde{b}_2 W^+)$. Since the W boson is relatively light, also the latter channel is open. In Fig. 10 the results for $\tilde{t}_2 \to \tilde{b}_1 W^+$ are shown, in Fig. 11 the ones for $\tilde{t}_2 \to \tilde{b}_2 W^+$. The divergences visible in the various plots are the same ones as found in the respective plot for $\Gamma(\tilde{t}_2 \to \tilde{b}_1 H^+)$. An additional (finite) dip is visible in the lower left plot of Fig. 10 in S2 for $|\mu| \approx 521$ GeV, due to an interplay of $t/\tilde{\chi}_2^\pm$ contributions to $\Sigma_{\tilde{b}_{11}}(m_{\tilde{b}_1})$, similar to the structure discussed for Fig. 5. In this part of the parameter space the results calculated within the renormalization scheme RS2 have to be discarded.

Overall, the loop corrections to $\Gamma(\tilde{t}_2 \to \tilde{b}_1 W^+)$ calculated within the renormalization scheme RS2 behave similar to the ones to $\Gamma(\tilde{t}_2 \to \tilde{b}_1 H^+)$. The size is relatively small, i.e. $\lesssim 20\%$ and $\lesssim 30\%$ of the tree-level results in the upper left and in the upper right plot of Fig. 10, respectively, for the regions which are not in conflict

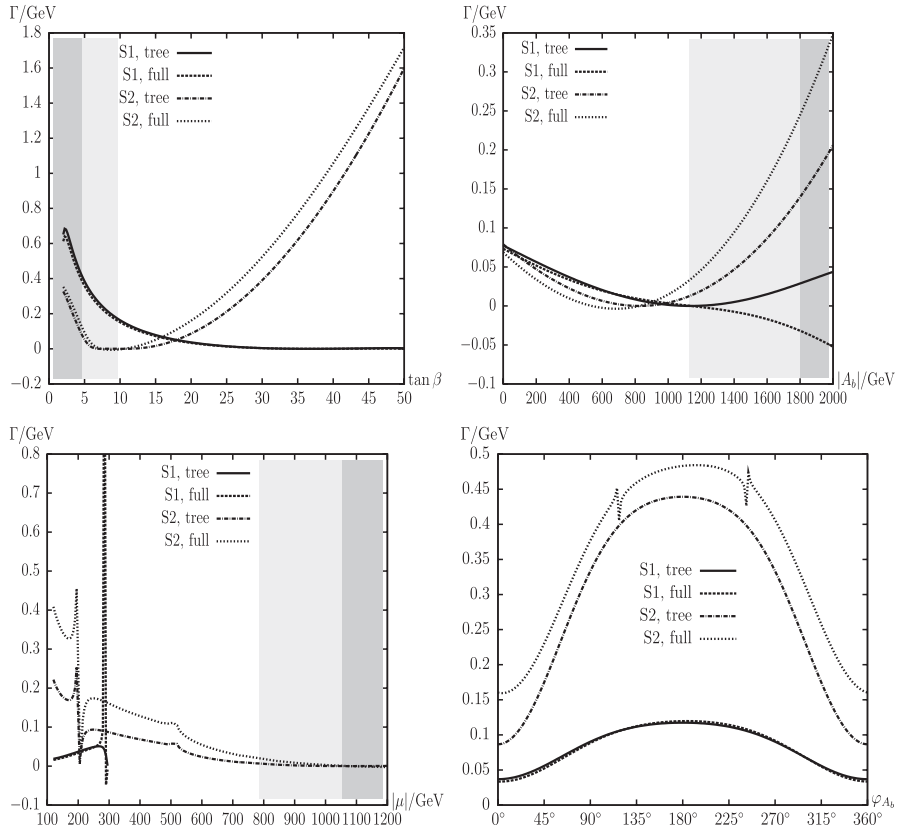

FIG. 9. $\Gamma(\tilde{t}_2 \to \tilde{b}_2 H^+)$. Tree-level and full one-loop corrected partial decay widths for the renormalization scheme RS2. The parameters are chosen according to the scenarios S1 and S2 (see Table II). For S1 the grey region is excluded and for S2 the dark grey region is excluded. Upper left plot: $\tan\beta$ varied. Upper right plot: $\tan\beta = 20$ and $|A_b|$ varied. Lower left plot: $\tan\beta = 20$ and $|\mu|$ varied. Lower right plot: $\tan\beta = 20$ and φ_{A_b} varied.

with charge- or color-breaking minima (for $|A_b| = 2000$ GeV a correction of $\sim$70% of the tree-level result can be observed in S1 due to the smallness of the tree-level value). We find loop corrections of the size of $\lesssim 20\%$ of the tree-level results in the lower left plot of Fig. 10 except for very small values of $|\mu|$ and in the lower right plot of Fig. 10. In the latter plot for S2 the known divergences appear at $\varphi_{A_b} \approx 117°, 243°$, leading to larger loop corrections for intermediate values of φ_{A_b}. Apart from the latter case the full one-loop corrections to $\Gamma(\tilde{t}_2 \to \tilde{b}_1 W^+)$ are well under control employing the renormalization scheme RS2.

Similar observations hold for the decay $\tilde{t}_2 \to \tilde{b}_2 W^+$, as shown in Fig. 11. In the upper left plot of Fig. 11 in the scenario S2 for $\tan\beta = |A_b|/|\mu| \approx 5.3$, the tree-level partial decay width vanishes, leading to a "negative value at the loop level." As discussed above, in this case also $|\mathcal{M}_{\text{loop}}|^2$ would have to be taken into account, yielding a positive value for $\Gamma(\tilde{t}_2 \to \tilde{b}_2 W^+)$. (A similar situation is found in the lower left plot of Fig. 11 for $|\mu| \approx 200$ GeV.) For somewhat larger $\tan\beta$ values, loop corrections of $\sim$50% of the tree-level values are reached, while in S1 they stay below $\sim$23% of the tree-level results. In the upper right plot of Fig. 11 the loop corrections are smaller than $\sim$40% of the tree-level values, depending on the size of $|A_b|$, see above. The loop corrections shown in the lower left plot of Fig. 11 yield maximal $\sim$9(37)% of the tree-level results in S1 (S2), apart from very small μ values, where the tree-level partial decay width can become accidentally small.

Finally, looking at the dependence on φ_{A_b} in the lower right plot of Fig. 11, apart from the known divergences in S2 around $\varphi_{A_b} \approx 117°, 243°$, the loop corrections do not exceed $\sim$6% and $\sim$35% of the tree-level values in S1 and in S2, respectively. Overall, except for the small parameter regions around $\varphi_{A_b} \approx 117°, 243°$, the full one-loop corrections to $\Gamma(\tilde{t}_2 \to \tilde{b}_2 W^+)$ are well under control employing the renormalization scheme RS2.

B. Comparison with SQCD calculation

Often QCD corrections to SM or MSSM processes are considered as the leading higher-order contributions. However, it has also been observed for SM processes (e.g. in the case of WH and ZH production at the Tevatron and LHC [69], for $H + 2$ jet production at the LHC [70], or for the Higgs decay to four fermions in

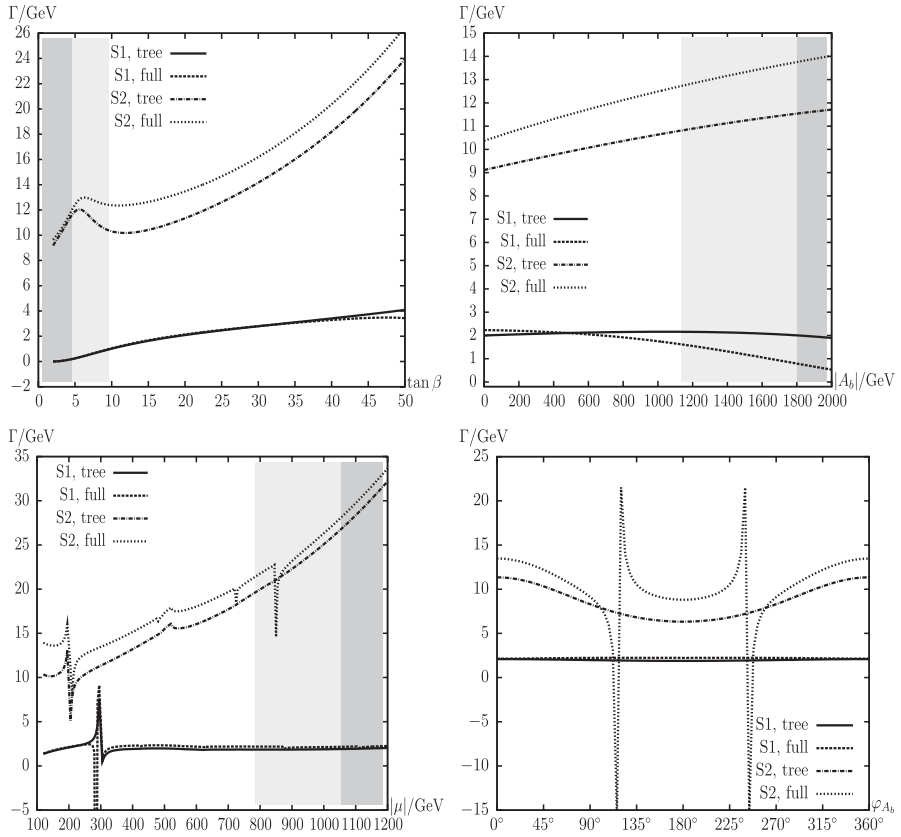

FIG. 10. $\Gamma(\tilde{t}_2 \to \tilde{b}_1 W^+)$. Tree-level and full one-loop corrected partial decay widths for the renormalization scheme RS2. The parameters are chosen according to the scenarios S1 and S2 (see Table II). For S1 the grey region is excluded and for S2 the dark grey region is excluded. Upper left plot: $\tan\beta$ varied. Upper right plot: $\tan\beta = 20$ and $|A_b|$ varied. Lower left plot: $\tan\beta = 20$ and $|\mu|$ varied. Lower right plot: $\tan\beta = 20$ and φ_{A_b} varied.

the SM [71]) that the electroweak corrections can be of similar size as the QCD corrections. Therefore, in the last step of our numerical evaluation, we show the size of the one-loop effects based on SUSY QCD (SQCD) only. The size of the SQCD corrections can then be compared to the full calculation presented in the previous subsection. It should be kept in mind that, following Eq. (44), also the masses of the scalar bottom quarks depend on the order of the calculation. Consequently, we do not explicitly compare SQCD with the full one-loop calculation, but analyze only the size and the sign of the pure SQCD corrections.

In Fig. 12 we show the tree-level values and SQCD one-loop corrected partial decay widths for $\tilde{t}_2 \to \tilde{b}_1 H^+$, $\tilde{t}_2 \to \tilde{b}_1 W^+$, $\tilde{t}_2 \to \tilde{b}_2 H^+$, $\tilde{t}_2 \to \tilde{b}_2 W^+$, respectively. The renormalization scheme RS2 is used, and hard gluon radiation is taken into account. The parameters are chosen according to S1 and S2 with $\tan\beta$ varied. For S1 and S2 the grey and the dark grey region is excluded via LEP Higgs searches, respectively. In the lower left plot of Fig. 12 the curves in S1 end at $\tan\beta \approx 27$ due to the closing of the phase space. The size of the SQCD one-loop corrections reaches the highest values for large $\tan\beta$ in the case of $\tilde{t}_2 \to \tilde{b}_{1,2} H^+$ and for intermediate $\tan\beta$ in the case of $\tilde{t}_2 \to \tilde{b}_{1,2} W^+$. The relative size in the percentage of the tree-level values do not exceed -8% in $\Gamma(\tilde{t}_2 \to \tilde{b}_1 H^+)$, $+18\%$ in $\Gamma(\tilde{t}_2 \to \tilde{b}_1 W^+)$, -24% in $\Gamma(\tilde{t}_2 \to \tilde{b}_2 H^+)$ and -6% in $\Gamma(\tilde{t}_2 \to \tilde{b}_2 W^+)$. The absolute size of the SQCD corrections can be compared with the upper left plots of Figs. 8–11, where the full one-loop corrections are shown. It becomes obvious, especially in S2, that restricting an evaluation to the pure SQCD corrections would strongly underestimate the full one-loop corrections. (Hard photon radiation can be as relevant as hard gluon radiation.) Consequently, the full set of one-loop corrections must be taken into account to yield a reliable prediction of the scalar top-quark decay width.

VII. CONCLUSIONS

A scalar top quark can decay into a scalar bottom quark and a charged Higgs boson or a W boson if the process is kinematically allowed. These decay modes can comprise a large part of the total stop decay width. The decay channels with a charged Higgs boson in the final state form a potentially important subprocess of cascade decays which are interesting for the search of charged Higgs bosons at the LHC. In order to arrive at a precise prediction of these

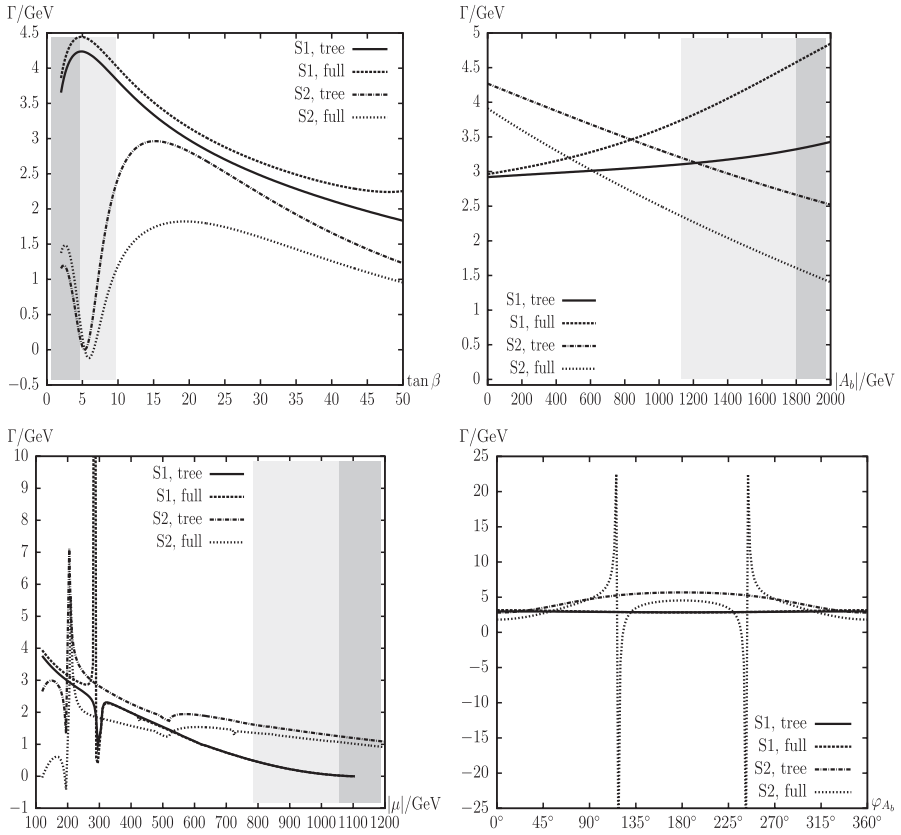

FIG. 11. $\Gamma(\tilde{t}_2 \to \tilde{b}_2 W^+)$. Tree-level and full one-loop corrected partial decay widths for the renormalization scheme RS2. The parameters are chosen according to the scenarios S1 and S2 (see Table II). For S1 the grey region is excluded and for S2 the dark grey region is excluded. Upper left plot: tanβ varied. Upper right plot: tan$\beta = 20$ and $|A_b|$ varied. Lower left plot: tan$\beta = 20$ and $|\mu|$ varied. Lower right plot: tan$\beta = 20$ and φ_{A_b} varied.

scalar top-quark partial decay widths at least a (full) one-loop calculation has to be performed. In such a calculation a renormalization procedure has to be applied that takes into account the top quark/squark as well as the bottom-quark/squark sector in the MSSM. These two sectors are connected via the soft SUSY-breaking mass parameter $M_{\tilde{Q}_L}$ of the superpartners of the left-handed quarks, which is the same in both sectors due to the $SU(2)_L$ invariance.

Within the MSSM with complex parameters (cMSSM) we defined six different renormalization schemes for the bottom quark/squark sector, while in the top quark/squark sector we applied a commonly used on-shell renormalization scheme, which is well suited for processes with external top and stop quarks. In our analysis we focused on the problem that, for certain parameter sets, an applied renormalization scheme might fail and cause large counterterm contributions that enhance the loop corrections to unphysically large values. We have analyzed analytically the drawbacks and shortcomings of each of the six renormalization schemes. Because of the relations between the parameters that have to be respected also at the one-loop level we did not find any renormalization scheme that results in reasonably small counterterm contributions over *all* the cMSSM parameter space we have analyzed (we did not consider a pure $\overline{\text{DR}}$ scheme which is not well suited to describe external particles). Some renormalization schemes (for instance, the "on-shell" scheme which is defined analogously to the one applied in the top quark/squark sector) fail over large parts of the parameter space. Others fail only in relatively small parts where, for instance, a divergence due to a vanishing denominator occurs. The most robust schemes turn out to be the "m_b, $A_b\overline{\text{DR}}$"(RS2) scheme and the "A_b vertex, ReY_b OS"(RS6) scheme. These renormalization schemes appear to be most suitable for higher-order corrections involving scalar top and bottom quarks.

We performed a detailed numerical analysis for the full one-loop result of the partial decay widths corresponding to the four processes $\tilde{t}_2 \to \tilde{b}_j H^+/W^+$ $(j = 1, 2)$ in our preferred scheme, "m_b, $A_b\overline{\text{DR}}$". The higher-order corrections, besides the full set of one-loop diagrams, also contain soft and hard QED and QCD radiation. We evaluated the higher-order predictions of the four partial decay widths as a function of tanβ, μ, A_b and φ_{A_b}. We found mainly modest corrections at the one-loop level. Larger corrections are mostly found in regions of the parameter space that are disfavored by experimental constraints

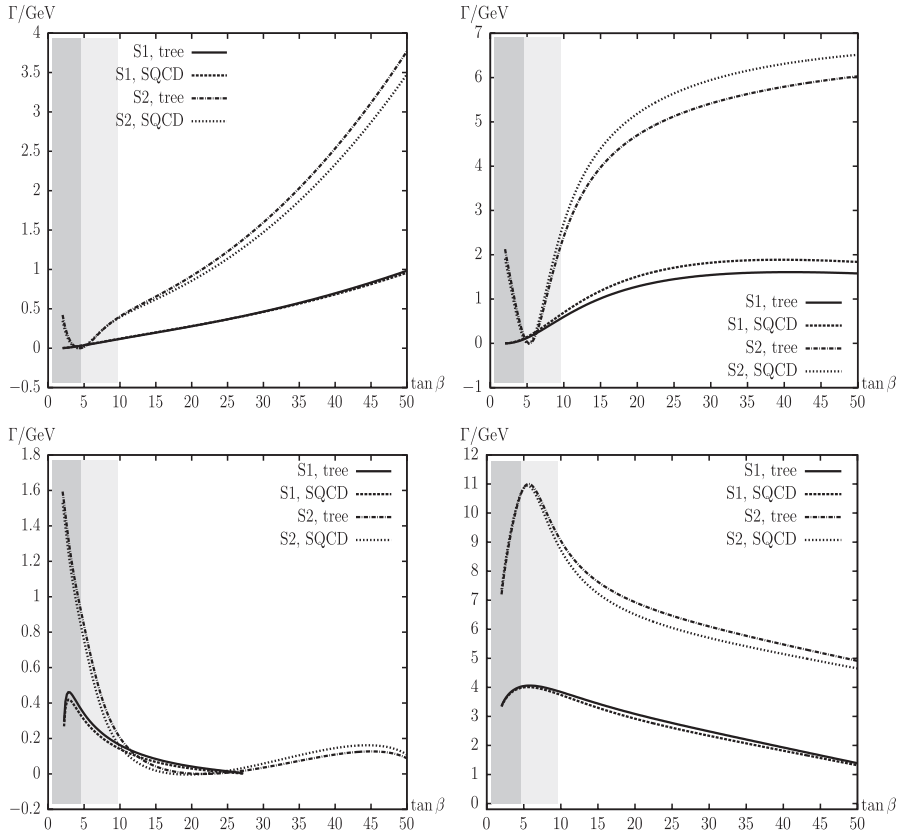

FIG. 12. Tree-level and SQCD corrected partial decay widths for the renormalization scheme RS2 with $\tan\beta$ varied. The parameters are chosen according to the scenarios S1 and S2 (see Table II). For S1 the grey region is excluded and for S2 the dark grey region is excluded. Upper left plot: $\Gamma(\tilde{t}_2 \to \tilde{b}_1 H^+)$. Upper right plot: $\Gamma(\tilde{t}_2 \to \tilde{b}_1 W^+)$. Lower left plot: $\Gamma(\tilde{t}_2 \to \tilde{b}_2 H^+)$. Lower right plot: $\Gamma(\tilde{t}_2 \to \tilde{b}_2 W^+)$.

and/or charge and color-breaking minima. A comparison of the full one-loop calculation with a pure SQCD calculation showed that the latter one can result in a very poor approximation of the full result and cannot be used for a reliable prediction.

A full one-loop calculation of the corresponding branching ratios requires the calculation of all possible partial decay widths of the scalar top quark (and consequently a renormalization of the full cMSSM) and will be presented elsewhere [26].

ACKNOWLEDGMENTS

We thank F. Campanario, S. Dittmaier, T. Fritzsche, J. Guasch, T. Hahn, W. Hollik, L. Mihaila, E. Mirabella, F. von der Pahlen, T. Plehn, M. Spira, D. Stöckinger, and G. Weiglein for helpful discussions. The work of S. H. was partially supported by the CICYT under Grant No. FPA 2007–66387. The work was supported in part by the European Community's Marie-Curie Research Training Network under Contract No. MRTN-CT-2006-035505 "Tools and Precision Calculations for Physics Discoveries at Colliders." H. R. acknowledges support by the Deutsche Forschungsgemeinschaft via the Sonderforschungsbereich/Transregio under Contract No. SFB/TR-9 "Computational Particle Physics" and the Initiative and Networking Fund of the Helmholtz Association under Contract No. HA-101 "Physics at the Terascale."

APPENDIX: *C* FUNCTIONS

As explained in Sec. IV F, in RS6 we have to deal with infrared divergent C functions (appearing in $\Lambda(p_1^2 = 0, p^2, p^2)$) with vanishing gram determinants. This case is not implemented in LOOPTOOLS [47]. Therefore we follow Ref. [40] (and references therein) and replace the corresponding C functions by well-behaving linear combinations of B functions.[9] For sake of completeness we briefly review our implementation. The class of C functions with only one external momentum zero, can be completely reduced to B functions. Having three different masses we can use partial fraction decomposition:

[9] FORMCALC [47] sorts the loop integrals with help of the masses. Consequently, any momentum can become zero, not only p_1. Furthermore, LOOPTOOLS uses a different convention than [40]: $C_1 = C_{11} - C_{12}$, $C_2 = C_{12}$.

$$C_0(0,\,p,\,p,\,m_1,\,m_2,\,m_3) = \frac{B_0(p,\,m_1,\,m_3) - B_0(p,\,m_2,\,m_3)}{m_1^2 - m_2^2}. \tag{A1}$$

With only two different masses applying partial differentiation (l'Hospital) yields

$$C_0(0,\,p,\,p,\,m_1,\,m_1,\,m_3) = \frac{\partial B_0(p,\,m_1,\,m_3)}{\partial(m_1^2)}. \tag{A2}$$

We also used symmetry relations and decompositions which can be found in [40] and the following shorthand notation:

$$D_{ij} = p^4 + m_i^4 + m_j^4 - 2(p^2 m_i^2 + p^2 m_j^2 + m_i^2 m_j^2). \tag{A3}$$

We included the following replacements of C_i functions with $p_1 = 0$:

$$C_0(0,\,p,\,p,\,m_1,\,m_2,\,m_3) \to \frac{B_0(p,\,m_1,\,m_3) - B_0(p,\,m_2,\,m_3)}{m_1^2 - m_2^2}, \tag{A4}$$

$$\begin{aligned} C_0(0,\,p,\,p,\,m_1,\,m_1,\,m_3) \to \frac{1}{D_{13}}[&(p^2 + m_3^2 - m_1^2) \\ &\times (2 - B_0(p,\,m_1,\,m_3)) \\ &+ (p^2 - m_3^2 - m_1^2)B_0(0,\,m_1,\,m_1) \\ &+ 2m_3^2 B_0(0,\,m_3,\,m_3)], \end{aligned} \tag{A5}$$

$$\begin{aligned} C_1(0,\,p,\,p,\,m_1,\,m_2,\,m_3) \to \frac{1}{3(m_1^2 - m_2^2)^2} \\ &\times [2m_1^2(B_0(p,\,m_2,\,m_3) - B_0(p,\,m_1,\,m_3)) \\ &+ (m_1^2 - m_2^2)B_0(p,\,m_2,\,m_3) - m_1^2 + m_2^2 \\ &+ (3m_1^2 - 2m_2^2 - m_3^2 + p^2)B_1(p,\,m_2,\,m_3) \\ &+ (m_3^2 - m_1^2 - p^2)B_1(p,\,m_1,\,m_3)], \end{aligned} \tag{A6}$$

$$C_2(0,\,p,\,p,\,m_1,\,m_2,\,m_3) \to \frac{B_1(p,\,m_1,\,m_3) - B_1(p,\,m_2,\,m_3)}{m_1^2 - m_2^2}, \tag{A7}$$

$$\begin{aligned} C_2(0,\,p,\,p,\,m_1,\,m_1,\,m_3) \to \frac{1}{2p^2}\Big\{&B_0(0,\,m_1,\,m_1) \\ &- B_0(p,\,m_1,\,m_3) - \frac{p^2 + m_1^2 - m_3^2}{D_{13}} \\ &\times [(p^2 - m_1^2 + m_3^2)(2 - B_0(p,\,m_1,\,m_3)) \\ &+ (p^2 - m_3^2 - m_1^2)B_0(0,\,m_1,\,m_1) \\ &+ 2m_3^2 B_0(0,\,m_3,\,m_3)]\Big\}. \end{aligned} \tag{A8}$$

In the case of $p_2 = 0$, we used the following replacements:

$$C_0(p,\,0,\,p,\,m_1,\,m_2,\,m_3) \to \frac{B_0(p,\,m_1,\,m_2) - B_0(p,\,m_1,\,m_3)}{m_2^2 - m_3^2}, \tag{A9}$$

$$\begin{aligned} C_0(p,\,0,\,p,\,m_1,\,m_2,\,m_2) \\ \to \frac{1}{D_{12}}[&(p^2 - m_2^2 + m_1^2)(2 - B_0(p,\,m_1,\,m_2)) \\ &+ (p^2 - m_1^2 - m_2^2)B_0(0,\,m_2,\,m_2) + 2m_1^2 B_0(0,\,m_1,\,m_1)], \end{aligned} \tag{A10}$$

$$\begin{aligned} C_1(p,\,0,\,p,\,m_1,\,m_2,\,m_3) \to \frac{1}{3(m_2^2 - m_3^2)^2} \\ &\times [2m_1^2(B_0(p,\,m_1,\,m_2) - B_0(p,\,m_1,\,m_3)) \\ &+ (m_2^2 - m_3^2)B_0(0,\,m_2,\,m_3) - m_3^2 + m_2^2 \\ &- (3m_3^2 - 2m_2^2 - m_1^2 - p^2)B_1(p,\,m_1,\,m_2) \\ &+ (m_3^2 - m_1^2 - p^2)B_1(p,\,m_1,\,m_3)], \end{aligned} \tag{A11}$$

$$\begin{aligned} C_2(p,\,0,\,p,\,m_1,\,m_2,\,m_3) \to \frac{1}{3(m_2^2 - m_3^2)^2} \\ &\times [2m_1^2(B_0(p,\,m_1,\,m_3) - B_0(p,\,m_1,\,m_2)) \\ &- (m_2^2 - m_3^2)B_0(0,\,m_2,\,m_3) + m_3^2 - m_2^2 \\ &- (3m_2^2 - 2m_3^2 - m_1^2 - p^2)B_1(p,\,m_1,\,m_3) \\ &+ (m_2^2 - m_1^2 - p^2)B_1(p,\,m_1,\,m_2)]. \end{aligned} \tag{A12}$$

Finally, for $p_3 = (p_1 + p_2) = 0$ we employed:

$$C_0(p,\,p,\,0,\,m_1,\,m_2,\,m_3) \to \frac{B_0(p,\,m_1,\,m_2) - B_0(p,\,m_2,\,m_3)}{m_1^2 - m_3^2}, \tag{A13}$$

$$\begin{aligned} C_0(p,\,p,\,0,\,m_1,\,m_2,\,m_1) \to \frac{1}{D_{12}}[&(p^2 - m_1^2 + m_2^2) \\ &\times (2 - B_0(p,\,m_1,\,m_2)) + (p^2 - m_2^2 - m_1^2)B_0(0,\,m_1,\,m_1) \\ &+ 2m_2^2 B_0(0,\,m_2,\,m_2)], \end{aligned} \tag{A14}$$

$$\begin{aligned} C_1(p,\,p,\,0,\,m_1,\,m_2,\,m_3) \\ \to \frac{B_0(p,\,m_2,\,m_3) + B_1(p,\,m_1,\,m_2) + B_1(p,\,m_2,\,m_3)}{m_1^2 - m_3^2}, \end{aligned} \tag{A15}$$

$$C_1(p,p,0,m_1,m_2,m_1) \to \frac{1}{2p^2}\Big\{B_0(0,m_1,m_1) - B_0(p,m_1,m_2) - \frac{p^2+m_1^2-m_2^2}{D_{12}}[(p^2-m_1^2+m_2^2) \times (2-B_0(p,m_1,m_2)) + (p^2-m_2^2-m_1^2)B_0(0,m_1,m_1) + 2m_2^2 B_0(0,m_2,m_2)]\Big\}, \quad \text{(A16)}$$

$$C_2(p,p,0,m_1,m_2,m_3) \to \frac{1}{3(m_1^2-m_3^2)^2} \times [2m_1^2(B_0(p,m_2,m_3) - B_0(p,m_1,m_2)) - (2m_1^2-m_2^2-m_3^2+p^2)B_0(p,m_2,m_3) + m_3^2 - m_1^2 - (3m_1^2-2m_3^2-m_2^2+p^2)B_1(p,m_2,m_3) + (m_2^2-m_1^2-p^2)B_1(p,m_1,m_2)]. \quad \text{(A17)}$$

[1] H. P. Nilles, Phys. Rep. **110**, 1 (1984); H. E. Haber and G. L. Kane, Phys. Rep. **117**, 75 (1985); R. Barbieri, Riv. Nuovo Cimento Soc. Ital. Fis. **11**, 1 (1988).
[2] A. Bartl, H. Eberl, K. Hidaka, S. Kraml, W. Majerotto, W. Porod, and Y. Yamada, Phys. Lett. B **419**, 243 (1998).
[3] A. Bartl, H. Eberl, K. Hidaka, S. Kraml, W. Majerotto, W. Porod, and Y. Yamada, Phys. Rev. D **59**, 115007 (1999).
[4] M. Mühlleitner, A. Djouadi, and Y. Mambrini, Comput. Phys. Commun. **168**, 46 (2005).
[5] L. Jin and C. Li, Phys. Rev. D **65**, 035007 (2002).
[6] C. Weber, H. Eberl, and W. Majerotto, Phys. Lett. B **572**, 56 (2003); Phys. Rev. D **68**, 093011 (2003).
[7] C. Weber, K. Kovarik, H. Eberl, and W. Majerotto, Nucl. Phys. **B776**, 138 (2007).
[8] J. Guasch, S. Peñaranda, and R. Sanchez-Florit, J. High Energy Phys. 04 (2009) 016.
[9] H. Rzehak, Ph.D. thesis, Technische Universität München, 2005.
[10] S. Heinemeyer, W. Hollik, H. Rzehak, and G. Weiglein, Eur. Phys. J. C **39**, 465 (2005).
[11] A. Brignole, G. Degrassi, P. Slavich, and F. Zwirner, Nucl. Phys. **B643**, 79 (2002).
[12] T. Fritzsche, Ph.D. thesis, Cuvillier Verlag, Göttingen, 2005.
[13] S. Heinemeyer, W. Hollik, H. Rzehak, and G. Weiglein, Phys. Lett. B **652**, 300 (2007).
[14] N. Baro and F. Boudjema, Phys. Rev. D **80**, 076010 (2009).
[15] A. Bartl, S. Hesselbach, K. Hidaka, T. Kernreiter, and W. Porod, Phys. Rev. D **70**, 035003 (2004).
[16] P. Langacker, G. Paz, L. Wang, and I. Yavin, J. High Energy Phys. 07 (2007) 055.
[17] A. Bartl, E. Christova, K. Hohenwarter-Sodek, and T. Kernreiter, Phys. Rev. D **70**, 095007 (2004).
[18] J. Ellis, F. Moortgat, G. Moortgat-Pick, J. Smillie, and J. Tattersall, Eur. Phys. J. C **60**, 633 (2009).
[19] F. Deppisch and O. Kittel, J. High Energy Phys. 09 (2009) 110; 03 (2010) 091(E).
[20] F. Deppisch and O. Kittel, J. High Energy Phys. 06 (2010) 67.
[21] H. Eberl, S. Frank, and W. Majerotto, arXiv:0912.4675.
[22] S. Heinemeyer, W. Hollik, and G. Weiglein, Comput. Phys. Commun. **124**, 76 (2000); see www.feynhiggs.de.
[23] S. Heinemeyer, W. Hollik, and G. Weiglein, Eur. Phys. J. C **9**, 343 (1999).
[24] G. Degrassi, S. Heinemeyer, W. Hollik, P. Slavich, and G. Weiglein, Eur. Phys. J. C **28**, 133 (2003).
[25] M. Frank, T. Hahn, S. Heinemeyer, W. Hollik, R. Rzehak, and G. Weiglein, J. High Energy Phys. 02 (2007) 047.
[26] T. Fritzsche, S. Heinemeyer, H. Rzehak, C. Schappacher, and G. Weiglein, "Heavy Stop Decays in the Complex MSSM: A Full One-Loop Analysis" (unpublished).
[27] T. Fritzsche and W. Hollik, Eur. Phys. J. C **24**, 619 (2002); T. Fritzsche, Diploma thesis, Universität Karlsruhe, 2000.
[28] A. Denner, Fortschr. Phys. **41**, 307 (1993).
[29] W. Hollik, E. Kraus, M. Roth, C. Rupp, K. Sibold, and D. Stöckinger, Nucl. Phys. **B639**, 3 (2002).
[30] W. Hollik and H. Rzehak, Eur. Phys. J. C **32**, 127 (2003).
[31] A. Djouadi, P. Gambino, S. Heinemeyer, W. Hollik, C. Jünger, and G. Weiglein, Phys. Rev. Lett. **78**, 3626 (1997); Phys. Rev. D **57**, 4179 (1998).
[32] J. Guasch, J. Sola, and W. Hollik, Phys. Lett. B **437**, 88 (1998).
[33] H. Eberl, S. Kraml, and W. Majerotto, J. High Energy Phys. 05 (1999) 016.
[34] A. Arhrib and R. Benbrik, Phys. Rev. D **71**, 095001 (2005).
[35] J. Guasch, W. Hollik, and J. Sola, Phys. Lett. B **510**, 211 (2001); J. High Energy Phys. 10 (2002) 040.
[36] Q. Li, L. Jin, and C. Li, Phys. Rev. D **66**, 115008 (2002).
[37] S. Kraml, H. Eberl, A. Bartl, W. Majerotto, and W. Porod, Phys. Lett. B **386**, 175 (1996); A. Djouadi, W. Hollik, and C. Jünger, Phys. Rev. D **55**, 6975 (1997).
[38] W. Beenakker, R. Höpker, and P. Zerwas, Phys. Lett. B **378**, 159 (1996).
[39] W. Beenakker, R. Höpker, T. Plehn, and P. Zerwas, Z. Phys. C **75**, 349 (1997).
[40] G. Devaraj and R. Stuart, Nucl. Phys. **B519**, 483 (1998).
[41] C. Amsler *et al.* (Particle Data Group), Phys. Lett. B **667**, 1 (2008).
[42] K. Chetyrkin and J. Kühn, Comput. Phys. Commun. **133**, 43 (2000).
[43] M. Carena, J. Ellis, A. Pilaftsis, and C. Wagner, Nucl. Phys. **B586**, 92 (2000); K. Williams, Ph.D. thesis, University of Durham, 2008.
[44] R. Hempfling, Phys. Rev. D **49**, 6168 (1994); L. Hall, R. Rattazzi, and U. Sarid, Phys. Rev. D **50**, 7048 (1994); M. Carena, M. Olechowski, S. Pokorski, and C. Wagner, Nucl. Phys. **B426**, 269 (1994).

[45] M. Carena, D. Garcia, U. Nierste, and C. Wagner, Nucl. Phys. **B577**, 88 (2000).

[46] J. Küblbeck, M. Böhm, and A. Denner, Comput. Phys. Commun. **60**, 165 (1990); T. Hahn, Comput. Phys. Commun. **140**, 418 (2001); T. Hahn and C. Schappacher, Comput. Phys. Commun. **143**, 54 (2002). The program and the user's guide are available via www.feynarts.de.

[47] T. Hahn and M. Pérez-Victoria, Comput. Phys. Commun. **118**, 153 (1999).

[48] F. del Aguila, A. Culatti, R. Munoz Tapia, and M. Perez-Victoria, Nucl. Phys. **B537**, 561 (1999).

[49] W. Siegel, Phys. Lett. **84B**, 193 (1979); D. Capper, D. Jones, and P. van Nieuwenhuizen, Nucl. Phys. **B167**, 479 (1980).

[50] D. Stöckinger, J. High Energy Phys. 03 (2005) 076.

[51] W. Hollik and D. Stöckinger, Phys. Lett. B **634**, 63 (2006).

[52] The couplings can be found in the files MSSM.ps.gz, MSSMQCD.ps.gz, and HMix.ps.gz as part of the FEYNARTS package [46].

[53] J. Frere, D. Jones, and S. Raby, Nucl. Phys. **B222**, 11 (1983); M. Claudson, L. Hall, and I. Hinchliffe, Nucl. Phys. **B228**, 501 (1983); C. Kounnas, A. Lahanas, D. Nanopoulos, and M. Quiros, Nucl. Phys. **B236**, 438 (1984); J. Gunion, H. Haber, and M. Sher, Nucl. Phys. **B306**, 1 (1988); J. Casas, A. Lleyda, and C. Munoz, Nucl. Phys. **B471**, 3 (1996); P. Langacker and N. Polonsky, Phys. Rev. D **50**, 2199 (1994); A. Strumia, Nucl. Phys. **B482**, 24 (1996).

[54] G. Abbiendi *et al.* LEP Higgs Working Group, Phys. Lett. B **565**, 61 (2003).

[55] LEP Higgs Working Group, Eur. Phys. J. C **47**, 547 (2006).

[56] S. Dimopoulos and S. Thomas, Nucl. Phys. **B465**, 23 (1996).

[57] M. Dugan, B. Grinstein, and L. Hall, Nucl. Phys. **B255**, 413 (1985).

[58] W. Hollik, J. Illana, S. Rigolin, and D. Stöckinger, Phys. Lett. B **416**, 345 (1998); **425**, 322 (1998).

[59] D. Demir, O. Lebedev, K. Olive, M. Pospelov, and A. Ritz, Nucl. Phys. **B680**, 339 (2004).

[60] D. Chang, W. Keung, and A. Pilaftsis, Phys. Rev. Lett. **82**, 900 (1999); **83**, 3972(E) (1999); A. Pilaftsis, Phys. Lett. B **471**, 174 (1999).

[61] O. Lebedev, K. Olive, M. Pospelov, and A. Ritz, Phys. Rev. D **70**, 016003 (2004).

[62] P. Nath, Phys. Rev. Lett. **66**, 2565 (1991); Y. Kizukuri and N. Oshimo, Phys. Rev. D **46**, 3025 (1992).

[63] T. Ibrahim and P. Nath, Phys. Lett. B **418**, 98 (1998); Phys. Rev. D **57**, 478 (1998); **58**, 019901(E) (1998); **60**, 079903(E) (1999); **60**, 119901(E) (1999); M. Brhlik, G. Good, and G. Kane, Phys. Rev. D **59**, 115004 (1999).

[64] S. Abel, S. Khalil, and O. Lebedev, Nucl. Phys. **B606**, 151 (2001).

[65] V. Barger, T. Falk, T. Han, J. Jiang, T. Li, and T. Plehn, Phys. Rev. D **64**, 056007 (2001).

[66] Y. Li, S. Profumo, and M. Ramsey-Musolf, J. High Energy Phys. 08 (2010) 62.

[67] H. Eberl, in *Loops & Legs 2010, Wörlitz, Germany, 2010: 10th Workshop on Elementary Particle Theory Organized by Theory Group, DESY, Zeuthen* (unpublished).

[68] ALEPH Collaboration, CDF Collaboration, D0 Collaboration, DELPHI Collaboration, L3 Collaboration, OPAL Collaboration, SLD Collaboration, LEP Electroweak Working Group, Tevatron Electroweak Working Group, and SLD Electroweak Heavy Flavour Groups, arXiv:0911.2604.

[69] M. Ciccolini, S. Dittmaier, and M. Krämer, Phys. Rev. D **68**, 073003 (2003).

[70] M. Ciccolini, A. Denner, and S. Dittmaier, Phys. Rev. Lett. **99**, 161803 (2007); Phys. Rev. D **77**, 013002 (2008).

[71] A. Bredenstein, A. Denner, S. Dittmaier, and M. Weber, J. High Energy Phys. 02 (2007) 080.